nature biomedical engineering

Article

https://doi.org/10.1038/s41551-023-01077-3

Bone-matrix mineralization dampens integrin-mediated mechanosignalling and metastatic progression in breast cancer

Received: 29 April 2022

Accepted: 30 June 2023

Published online: 07 August 2023

Check for updates

Siyoung Choi[1,6], Matthew A. Whitman[1,6], Adrian A. Shimpi[1], Nicole D. Sempertegui[1], Aaron E. Chiou[1], Joseph E. Druso[1], Akanksha Verma[2], Stephanie C. Lux[1], Zhu Cheng[3], Matthew Paszek[3], Olivier Elemento[2], Lara A. Estroff[4,5] ✉ & Claudia Fischbach[1,5] ✉

In patients with breast cancer, lower bone mineral density increases the risk of bone metastasis. Although the relationship between bone-matrix mineralization and tumour-cell phenotype in breast cancer is not well understood, mineralization-induced rigidity is thought to drive metastatic progression via increased cell-adhesion forces. Here, by using collagen-based matrices with adjustable intrafibrillar mineralization, we show that, unexpectedly, matrix mineralization dampens integrin-mediated mechanosignalling and induces a less proliferative stem-cell-like phenotype in breast cancer cells. In mice with xenografted decellularized physiological bone matrices seeded with human breast tumour cells, the presence of bone mineral reduced tumour growth and upregulated a gene-expression signature that is associated with longer metastasis-free survival in patients with breast cancer. Our findings suggest that bone-matrix changes in osteogenic niches regulate metastatic progression in breast cancer and that in vitro models of bone metastasis should integrate organic and inorganic matrix components to mimic physiological and pathologic mineralization.

Breast cancer frequently metastasizes to bone where it leads to osteolysis and poor clinical prognosis[1–3], but therapies to treat or prevent bone metastasis are lacking. Most previous research has focused on clinically apparent bone degradation uncovering that unbalanced osteoclast activity and consequential activation of the 'vicious cycle of bone metastasis' allow asymptomatic residual disease to develop into overt metastasis[4,5]. However, how tumour cells initially colonize and survive in the skeletal microenvironment is poorly understood. Indeed, tumour cells can disseminate to bone very early during tumour development and enter a state of latency in which they proliferate less and assume stem cell-like properties[6–8]. Activation of these latent tumour cells to a more proliferative phenotype contributes to their outgrowth into metastatic tumours after years or even decades. As microenvironmental conditions are key determinants of tumour-cell latency and stemness[7,9], it will be critical to better define how bone-specific niches and changes thereof influence the stem-like phenotype of tumour cells in the skeleton.

While most research on early-stage bone metastasis focuses on the marrow, tumour cells also colonize osteogenic niches in the skeleton. These niches consist of osteoblasts and their progenitors

[1]Nancy E. and Peter C. Meinig School of Biomedical Engineering, Cornell University, Ithaca, NY, USA. [2]Caryl and Israel Englander Institute for Precision Medicine, Institute for Computational Biomedicine, Weill Cornell Medicine, New York, NY, USA. [3]Robert Frederick Smith School of Chemical and Biomolecular Engineering, Cornell University, Ithaca, NY, USA. [4]Department of Materials Science and Engineering, Cornell University, Ithaca, NY, USA. [5]Kavli Institute at Cornell for Nanoscale Science, Cornell University, Ithaca, NY, USA. [6]These authors contributed equally: Siyoung Choi, Matthew A. Whitman. ✉e-mail: lae37@cornell.edu; cf99@cornell.edu

whose hallmark function is to deposit and mineralize extracellular matrix (ECM)[9,10] (Fig. 1a). Conditions affecting osteoblasts and their progenitors (such as aging or chemotherapy) inhibit the formation of mineralized matrix and alter the secretome of osteoblast-lineage cells[11,12]. While the secretome has been shown to regulate metastatic latency[13] and outgrowth[11,12], it remains underappreciated how varied bone ECM formation and mineralization influence tumour-cell phenotype. Better understanding these connections will be important as changes in the ECM play a key role in regulating tumour-cell phenotype because (1) disseminated cancer cells directly interact with the matrix[10,14] and (2) patients with breast cancer with decreased bone mineral density have a higher risk of developing bone metastasis[15,16].

During osteogenesis, osteoblasts first deposit osteoid, the collagen I-rich unmineralized component of bone ECM within which carbonated hydroxyapatite (HA; $Ca_{10}(PO_4CO_3)_6(OH)_2$) nanoparticles subsequently form[17,18] (Fig. 1a). This process of mineralization is accompanied by distinct changes in bone-matrix mechanical properties (such as increased stiffness and reduced stress relaxation[19]), which can impact tumour-cell phenotype through altered mechanosignalling[20–22]. Moreover, bone-matrix mineralization is a dynamic process that changes as a function of anatomical site, age, diet and disease[23–26]. How changes in bone-matrix mineralization influence the phenotype of tumour cells, however, remains unclear due in part to a lack of model systems that allow selective control over bone-matrix mineral content for mechanistic studies. Studies with such systems will be critical to elucidate why reduced bone formation and local mineral density increase the risk for bone metastasis[12,27], whereas conditions promoting new bone formation and mineralization inhibit bone metastasis[28,29].

Conventional models of breast cancer (that is, two-dimensional cell culture and mouse models) fail to (1) recapitulate compositional, structural and mechanical alterations of bone matrix and (2) allow control over the level of mineralization that changes during osteogenesis and in response to conditions that correlate with increased risk for bone metastasis (in particular, age, vitamin D deficiency and premetastatic bone remodelling)[24,25,30,31]. More advanced methods such as culturing fragments of tumour-cell-containing mouse bones ex vivo can recapitulate tumour-cell interactions with bone matrix in the presence of bone-resident tumour cells, but matrix mineralization cannot be controlled independently in this system[32]. While many protocols have been developed to mineralize biomaterials for cell culture studies or regenerative applications, most of these methods deposit HA on top of substrates rather than mimicking physiological mineralization. Yet, bone matrix is a composite material whose unique mechanical properties are determined by HA-enforced collagen fibres that form by intrafibrillar nucleation of the mineral phase within the organic matrix[19,33].

Here we report the development of osteoid-like and bone-like scaffolds in which we can selectively adjust bone-matrix mineral content for both in vitro and in vivo experiments in a physiologically relevant manner. These model systems include: (1) 2.5D collagen matrices in which we synthetically induce bone-like intrafibrillar mineralization through a modified polymer-induced liquid precursor (PILP) method[34] and (2) decellularized trabecular bone scaffolds in which we can selectively remove mineral without affecting organic ECM composition and microstructure. Using these biofunctional scaffolds, we probed the role of bone-matrix mineralization in regulating the phenotype of breast cancer cells in vitro and tested which role mechanosignalling plays in this process. Then, we evaluated the impact of our results on tumour growth in mice and on patient prognosis using bioinformatic analyses of published clinical data sets. Collectively, our results suggest that the mineral content of bone matrix regulates skeletal metastasis by influencing the phenotype of breast cancer cells. These findings underscore that bone matrix is an important component of the osteogenic niche that can impact bone metastasis and should thus be considered when designing model systems for studies of breast-cancer bone metastasis.

Results

Mineralizing bone niches attract tumour cells and can be mimicked in vitro

Whether disseminated tumour cells localize to skeletal regions of new matrix mineralization is poorly characterized given the intrinsic difficulty of imaging rare numbers of tumour cells within fully intact, highly autofluorescent mineralized bones. To circumvent this challenge, we labelled MDA-MB231 breast cancer cells with bright fluorescent silica nanoparticles and intracardially injected them into athymic nude mice in which newly mineralizing bone surfaces were labelled with calcein[35]. As expected, cancer cells localized to niches within the marrow in this model[36]. However, light-sheet microscopy of cleared mouse tibiae also revealed that tumour cells co-localized with regions of new matrix mineralization (Fig. 1b), consistent with previous results identifying the osteogenic niche as a target for early-stage bone colonization[10].

To investigate whether bone-matrix mineralization alone affects the phenotype of tumour cells, we used a bone-like ECM system in which we induced biofunctional intrafibrillar mineralization of collagen using a modified PILP method[34,37]. We chose collagen type I for this system as osteoid primarily consists of collagen type I and because bone-matrix mineralization primarily occurs in collagen type I fibres[38]. Briefly, collagen was cast into polydimethylsiloxane (PDMS) microwells or on glass coverslips and mineralized in a solution containing calcium and phosphate ions as well as polyaspartic acid (PAA) to control the formation of HA nanocrystals within collagen fibrils (Fig. 1c). In this system, the PAA serves a function similar to non-collagenous proteins in bone, resulting in the formation of bone-like mineralized collagen fibres[20]. Scanning electron microscopy (SEM) image analysis confirmed that mineralization did not impact the fibrous architecture of collagen but increased the thickness of individual fibrils (Fig. 1d,e) due to mineral formation as confirmed by backscattered electron (BSE) imaging (Fig. 1d). Fourier transform infrared (FT-IR) spectroscopy and powder X-ray diffraction (pXRD) further identified that the chemical composition and phase of the newly formed mineral were consistent with HA (Fig. 1f,g). The FT-IR spectra of both control and mineralized collagen contained characteristic protein amide peaks between 1,200–1,700 cm^{-1}, while PO_4^{3-} peaks indicative of HA (500–700 cm^{-1} and 900–1,200 cm^{-1}) were only detected in mineralized collagen (Fig. 1f). Moreover, the mineral content of these matrices was comparable to that of human bone as suggested by FT-IR analysis of the mineral to matrix ratio (Extended Data Fig. 1; mineralized collagen: ~4; human bone: 3–6)[26]. The phase of the mineral that formed in collagen was similar to the poorly crystalline, non-stoichiometric carbonated apatite in bone[39] as indicated by the presence and broadening of pXRD peaks at 26° and 32° (Fig. 1g). Collagen is a viscoelastic material that undergoes nonlinear elastic changes upon deformation. Upon mineralization, the nonlinear elastic response of the collagen will change, hence cellular behaviour is also likely to change[40]. Indeed, mineralization increases the storage and loss moduli of collagen, indicating increased stiffness as expected (Extended Data Fig. 2). In addition, rheological analysis revealed that mineralization prevents collagen strain stiffening while reducing collagen stress relaxation in response to strain (Fig. 1h,i). Taken together, these results indicate that bone-like collagen-HA composites can be formed by synthetic intrafibrillar collagen mineralization and that the resulting substrates are characterized by altered chemical, physical and mechanical properties.

Collagen mineralization alters tumour-cell gene expression and growth

As microfabricated collagen and mineralized collagen substrates recapitulated the two extremes of bone-matrix mineralization (that is, non-mineralized osteoid versus mineralized bone matrix), we next used these materials to test how bone-matrix mineralization affects tumour-cell phenotype. When cultured on mineralized versus control collagen, metastatic MDA-MB231 breast cancer cells spread less,

https://doi.org/10.1038/s41551-023-01077-3

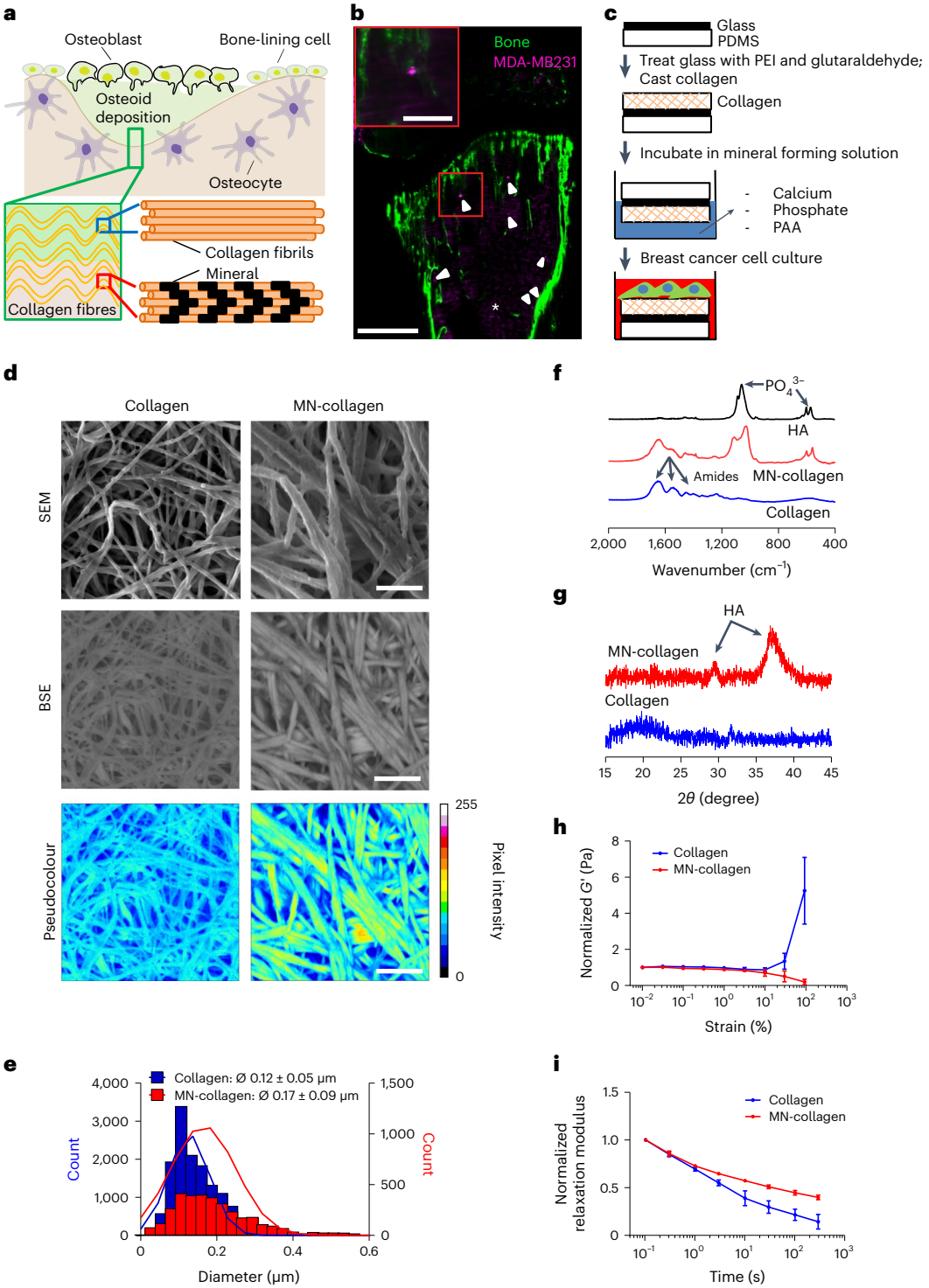

Fig. 1 | Engineered bone-matrix models to study tumour cell interactions with mineralized collagen. a, Schematic of bone ECM formation in osteogenic niches. Osteoblasts first deposit osteoid, which consists primarily of collagen type I fibres (blue box) that become mineralized (red box) over time by intrafibrillar mineralization. **b**, Intracardially injected MDA-MB231 labelled with Cy5-containing silica nanoparticles (magenta) disseminate to regions in which new bone matrix becomes mineralized, as visualized by light-sheet imaging of a calcein-labelled cleared mouse tibia (green). White arrowheads and asterisk indicate MDA-MB231 cells and autofluorescence of bone marrow, respectively. Scale bar, 600 µm and 150 µm (inset). **c**, Experimental setup to mineralize fibrillar collagen type I matrices via the PILP method for subsequent analysis of breast cancer-cell phenotype. **d**, Representative SEM and BSE images visualizing the fibrillar nature and mineral content of collagen and mineralized collagen (MN-collagen) substrates. Pseudocolour indicates mineral content as determined from BSE images by converting grey-scale pixel intensity to a linear 256-bit colour scale. Scale bar, 1 µm. **e**, Fibril diameter (Ø) of control and mineralized collagen substrates quantified from SEM images. **f**, FT-IR spectra of the different collagen substrates and highly crystalline HA particles as control. Arrows indicate phosphate (450–750 cm^{-1} and 900–1,300 cm^{-1}) and amide peak areas (1,200–1,700 cm^{-1}). **g**, pXRD patterns indicate the presence of HA in mineralized, but not control collagen. **h**, Strain stiffening of collagen and mineralized collagen. Strain sweeps with normalized storage modulus (G') ($n = 3$). **i**, Stress relaxation of collagen and mineralized collagen. Time sweeps with normalized relaxation modulus for stress relaxation ($n = 3$). Data are mean ± s.d.

were rounder and exhibited reduced remodelling of their surrounding collagen network as indicated by limited fibre alignment and densification that are known to mediate local strain stiffening in control collagen[41] (Fig. 2a,b). Consistent with these morphological differences, principal component analysis (PCA) of bulk RNA-seq data sets suggested that collagen mineralization globally affects gene expression of MDA-MB231 (Fig. 2c). Differential gene expression analysis further identified that genes associated with breast cancer metastasis (*ANGPTL2, CAMK1D, CEMIP*)[42–44] and stemness (*B4GALNT3, TRIB3*)[45,46] were among the top 50 differentially expressed genes in the mineralized collagen condition, while most of the top 50 ranked genes regulated by collagen were linked with the cell cycle (*CDCA7, CHTF18, DBF4B, KIF18B*) (Fig. 2d, Supplementary Table 1 and Extended Data Fig. 3). Gene set enrichment analysis (GSEA) confirmed that cell cycle-related gene sets, most prominently those related to DNA replication, were over-represented in cells cultured on collagen, while gene sets associated with stress response and ECM disassembly, transcription and cell migration were over-represented in cells cultured on mineralized collagen (Fig. 2e and Extended Data Fig. 4). These results suggest that bone-matrix mineralization impacts breast cancer cell functions centrally implicated in bone metastasis.

As gene sets related to cell-cycle pathways were most prominently affected by changes in collagen mineralization, we next measured tumour-cell growth on the different substrates. Both MDA-MB231 Ki67 positivity and bromodeoxyuridine (BrdU) incorporation as well as DNA content were reduced by culture on mineralized collagen relative to collagen, indicating that collagen mineralization decreases tumour-cell proliferation (Fig. 2f,g and Supplementary Fig. 1). Accordingly, collagen mineralization reduced growth of the bone tropic MDA-MB231 subclones BoM1-2287 and BoM-1833 (ref. 20) and oestrogen-receptor-positive MCF7 cells, supporting that our findings were not limited to MDA-MB231 (Fig. 2g). Patients with metastatic breast cancer have high plasma fibronectin concentrations (300 μg ml^{-1}) and fibronectin is readily adsorbed onto the bone mineral HA[47,48]. However, differences in fibronectin adsorption did not contribute to our results as validated in a control experiment in which we pre-adsorbed relevant fibronectin concentrations to the different substrates (Extended Data Fig. 5). Next, we evaluated whether this decreased proliferative state is reversible in scenarios that lead to decreased matrix mineralization (such as aging, chemotherapy and osteolysis)[24,25,49]. To this end, we precultured MDA-MB231 on collagen and mineralized collagen for 7 d, a timeframe reported to cause irreversible phenotypic changes[50,51] and then reseeded them onto either collagen or mineralized collagen (Fig. 2h). Indeed, cells precultured on mineralized collagen assumed a more proliferative phenotype when reseeded onto non-mineralized collagen, albeit at reduced levels relative to cells that were precultured on collagen. In contrast, reseeding cells onto mineralized collagen significantly decreased tumour-cell growth irrespective of the substrate on which cells were cultured previously (Fig. 2h). These data indicate that collagen mineralization reduces tumour-cell growth in a reversible manner, suggesting that quiescent cells may develop into proliferative lesions as matrix mineralization changes.

In osteogenic niches in vivo, tumour cells not only interact with matrix but also with osteoblasts and their progenitors. Therefore, we next validated that increased matrix mineralization correlates with decreased tumour-cell growth in the presence of bone-resident cells. Indeed, MDA-MB231 co-cultured with human bone marrow-derived mesenchymal cells (hMSCs) that had deposited mineralized matrix grew less than tumour cells co-cultured with hMSCs that failed to mineralize matrix (Extended Data Fig. 6a). While varied mineralization in these co-culture experiments was mimicked by the presence or absence of osteogenic media, similar scenarios may occur in vivo because tumour cells secrete factors that alter bone growth[52,53] and inhibit the formation of mineralized bone matrix by hMSCs (Extended Data Fig. 6b). Importantly, in scenarios where mineral matrix formation by hMSCs was inhibited (either by lack of osteogenic factors or the presence of tumour-secreted factors), hMSC deposited increased amounts of fibronectin (Extended Data Fig. 6c), a matrix protein that can independently promote bone metastasis and may thus exaggerate differences in scenarios in which bone-matrix formation is inhibited in vivo. Collectively, these results suggest that changes in bone-matrix mineralization correlate with altered tumour-cell growth and are relevant or even amplified in the presence of bone-resident cells.

Mineralized collagen increases stemness in breast cancer cells

Motivated by our observation that collagen mineralization reduces tumour-cell proliferation (Fig. 2), a hallmark of quiescent stem-like tumour cells[7,8] and because dissemination to bone confers stem-like properties on cancer cells[54], we next determined whether mineralized collagen regulates the stem-like phenotype of breast cancer cells. These experiments were performed with an MDA-MB231 stem cell reporter cell line that expresses green fluorescent protein (GFP) as a function of Nanog promoter activity[55], which we validated to correlate with protein level of two other stem-cell markers, Oct4 and Sox2 (Fig. 3a and Supplementary Fig. 2). Flow cytometry and confocal image analysis indicated that culture on mineralized collagen increased the number of GFP^{high} cells relative to culture on collagen or polystyrene (PS) (Fig. 3b,c). To confirm that these changes were driven by mineral, we performed a dose response study in which substrates of controlled HA content were fabricated by dissolving HA from fully mineralized collagen at physiological pH for up to 6 d, a process that selectively removed HA without affecting collagen microstructure (Fig. 3d and Extended Data Fig. 7). Decreasing mineral content reduced the percentage of Nanog-GFP-positive cells, supporting that collagen mineralization directly regulates the stem-like phenotype of breast cancer cells (Fig. 3e). Further validating the induction of stemness by mineral, parental MDA-MB231 cultured on mineralized collagen also exhibited increased activity of the stem-cell marker aldehyde dehydrogenase (ALDH)[56,57] (Fig. 3f). Moreover, MDA-MB231 precultured on mineralized collagen formed more colonies in soft agar relative to the same cells precultured on PS or collagen, indicating that interactions with

Fig. 2 | Mineralization of collagen alters breast cancer cell gene expression and growth. a, MDA-MB231 morphology and collagen network structure 5 h after seeding, visualized via confocal reflectance microscopy (left) and analysis of projected cell area and aspect ratio (right) (at least 221 cells examined over $n = 4$; $^{***}P < 0.0001$; $^{\#\#\#}P < 0.0001$). Scale bar, 20 μm. **b**, Pseudocoloured reflectance intensity maps indicate differences in collagen remodelling between both conditions by converting grey-scale pixel intensity to a linear 256-bit colour scale. Scale bar, 20 μm. **c**–**e**, Effect of collagen mineralization on MDA-MB231 gene expression determined by PCA (**c**), differential gene expression analysis ($n = 4$) (**d**) and GSEA (**e**) of bulk RNA-seq data collected after 7 d of culture on the different substrates. In **d**, genes coloured in red are upregulated in cells cultured on mineralized collagen, while genes coloured in blue are upregulated on collagen. For GSEA, the top 10 enriched pathways in cells cultured on collagen and mineralized collagen were derived from GO biological processes. Green dots indicate FDRs. Normalized enrichment scores are denoted by NES. **f**, Representative confocal micrographs (top) and corresponding quantification of $Ki67^+$ MDA-MB231 cells (bottom) ($n = 4$; $^{***}P = 0.0002$). Scale bar, 50 μm. **g**, Fluorimetric quantification of DNA content of breast cancer cell lines cultured for 7 d on the different substrates ($n = 4$; $^{**}P = 0.0090$; $^{***}P = 0.0004$; $^{\#\#}P = 0.0042$; $^{\#\#\#}P < 0.0001$). **h**, Analysis of MDA-MB231 growth following 7 d of preculture on the different substrates ($n = 4$; $^{**}P = 0.0016$; $^{\#\#}P = 0.0015$; $^{****}P < 0.0001$; $^{\#\#\#\#}P < 0.0001$; $^{++++}P < 0.0001$). Data are mean ± s.d. Statistical differences were determined using two-tailed unpaired *t*-test with Welch's correction for data in **a**, two-tailed unpaired *t*-test for data in **f** and **g**, and two-way ANOVA with Sidak's multiple comparisons test for data in **h**.

https://doi.org/10.1038/s41551-023-01077-3

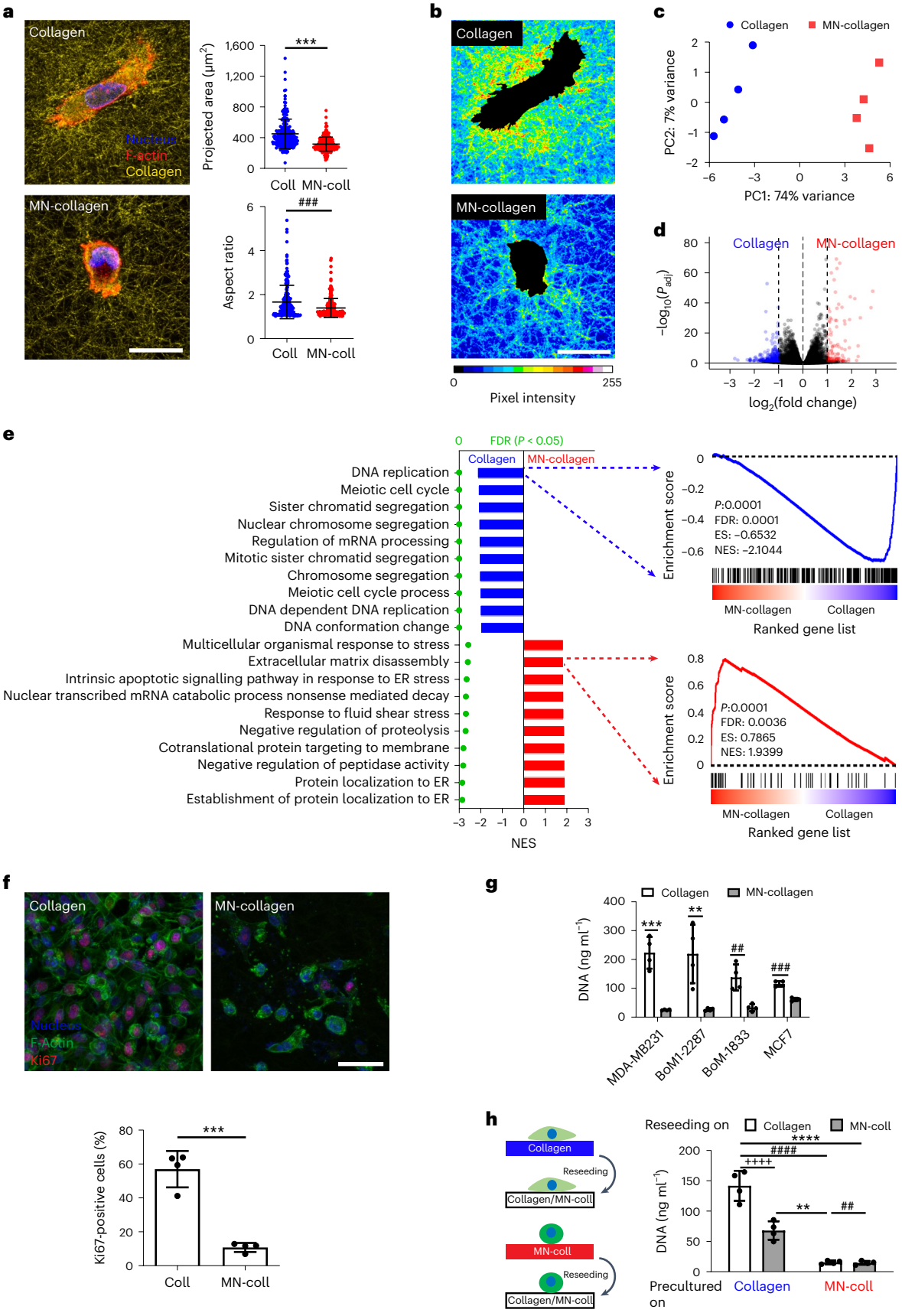

https://doi.org/10.1038/s41551-023-01077-3

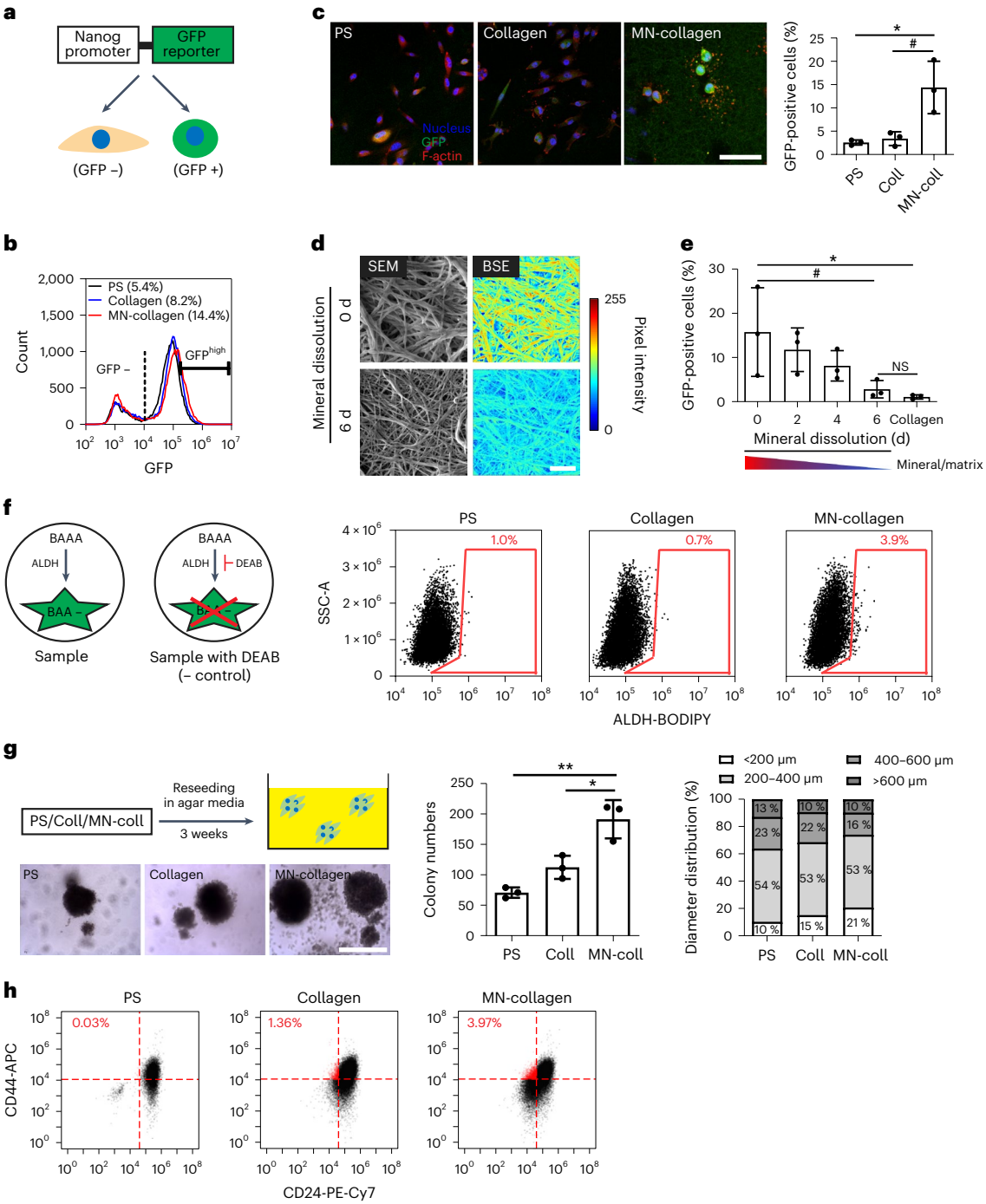

Fig. 3 | Collagen mineralization induces a stem-like phenotype in breast cancer cells. a, Schematic of the Nanog-MDA-MB231 reporter cell line in which increased GFP expression indicates a more stem-like phenotype. **b**, Flow cytometry analysis of Nanog-MDA-MB231 reporter cells after 7 d of culture on PS, collagen or mineralized collagen. **c**, Representative confocal micrographs (left) and corresponding quantification of GFP-positive cells (right) after 7 d of culture on the different substrates ($n = 3$; $^{*}P = 0.0122$; $^{\#}P = 0.0170$). Scale bar, 100 µm. **d**, Representative SEM and BSE (pseudocoloured) images of mineralized collagen at different timepoints of dissolution. Pseudocolour indicates mineral content as determined from BSE images by converting grey-scale pixel intensity to a linear 256-bit colour scale. Scale bar, 2 µm. **e**, Confocal image analysis of GFP-positive cells as a function of collagen mineral content ($n = 3$; $^{*}P = 0.0221$; $^{\#}P = 0.0427$; NS, not significant). Mineral content of substrates was controlled by dissolution of HA over several days. **f**, Analysis of ALDH activity in parental MDA-MB231 cells. Aminoacetaldehyde (BAAA) is converted by ALDH into BODIPY-aminoacetate (BAA) that leads to increased intracellular fluorescence. Diethylaminobenzaldehyde (DEAB) inhibits ALDH and is labelled as negative control. **g**, Soft agar colony formation (left) after preculture of parental MDA-MB231 on the different substrates. Scale bar, 400 µm. Quantification of the number (middle) and size distribution (right) of colonies larger than 100 µm in diameter ($n = 3$; $^{*}P = 0.0104$; $^{**}P = 0.0012$). **h**, Co-expression of CD44 and CD24 in MCF7 after 7 d of culture. The percentage of $CD44^{+}/CD24^{-}$ cells is indicated at the upper left of each panel. Data are mean ± s.d. Statistical differences were determined using one-way ANOVA with Tukey's multiple comparisons test for data in **c** and **g**, and one-way ANOVA with Dunnett's multiple comparisons test for data in **e**.

mineralized collagen endow tumour cells with survival advantages in adhesion-independent scenarios (Fig. 3g). Bioinformatic analysis of our RNA-seq data set suggested that upregulation of *FOXD3* target genes may be involved, these target genes coding for transcription factors that regulate stem cell pluripotency and self-renewal[58,59], reduce proliferation of breast cancer cells and predict better survival[60] (Extended Data Fig. 4a,b).

To determine whether our findings were limited to MDA-MB231 cells, we also tested BoM-1833; however, given the intrinsically high proliferative capacity of these cells, their fraction of ALDH-positive cells was negligible regardless of cell culture substrate (Supplementary Fig. 3). In contrast, MCF7 increased their stem-like properties following culture on mineralized collagen as demonstrated by a higher number of $CD44^+/CD24^-$ cells (Fig. 3h). For MCF7, $CD44^+/CD24^-$ cells represent appropriate stemness markers and characterize a population with more mesenchymal characteristics[61], while ALDH is better suited for MDA-MB231 and BoM-1833 as almost all cells in these two lines are $CD44^+/CD24^-$ (ref. 61). Consistent with a more mesenchymal phenotype, MCF7 cells cultured on mineralized collagen also formed fewer cell–cell adhesions and had reduced E-cadherin levels (Extended Data Fig. 8).

Mineralized collagen regulates breast cancer cell mechanosignalling

Increased cell-adhesion forces are drivers of tumour-cell growth and typically increase on stiffer matrices[62]. While mineralization increases collagen stiffness, it simultaneously reduces collagen strain stiffening and stress relaxation, resulting in decreased rather than increased cell-adhesion forces, with consequential changes in cell spreading and collagen network remodelling (Figs. 1h,i and 2a,b)[19,20,63]. Because of these connections, we hypothesized that mineral-induced changes in mechanosignalling may be responsible for the above-described changes in tumour-cell phenotype. To define which role mineralization-dependent changes in mechanotransduction play in regulating tumour-cell growth, we cultured MDA-MB231 on collagen and mineralized collagen in the presence and absence of β1-integrin-blocking antibodies and pharmacological inhibitors of focal adhesion kinase (FAK) (FAK inhibitor 14), Rho-associated protein kinase (ROCK, Y27632) and phosphoinositide 3-kinase (PI3K, LY294002) (Fig. 4a). Treatment with these reagents reduced tumour-cell growth on collagen as expected but had no effect on mineralized collagen, suggesting that tumour-cell mechanosignalling may be reduced on mineralized collagen. Tumour cells interacting with collagen have been described to increase their adhesion forces by aligning collagen fibres in a process that activates mechanosignalling via a positive feedback mechanism[41]. To test whether collagen mineralization interferes with this process by preventing cell-mediated collagen network remodelling and strain stiffening as described above (Figs. 1h and 2b) and thus, reciprocal activation of cellular adhesion forces[20], we performed traction force microscopy. Indeed, consistent with the limited effect of mechanosignalling inhibitors on tumour growth, MDA-MB231 precultured on mineralized collagen exhibited reduced cellular traction forces relative to their counterparts precultured on collagen or PS (Fig. 4b and Extended Data Fig. 9), and sorted GFP^{high} cells exhibited similarly reduced traction forces relative to GFP^{low} cells (Fig. 4c). Consistent with these differences, MDA-MB231 cultured on mineralized versus control collagen adjusted their expression of genes related to cytoskeletal remodelling including *NEDD9* (a focal adhesion protein regulating cell attachment and the cell cycle), *KRT19* (intermediate filament proteins keratin), *S100A4* (encoding S100 proteins that regulate cell cycle progression and differentiation) and *FN1* (encoding fibronectin, which broadly regulates adhesion, but also dormancy)[64] (Extended Data Fig. 4a,c).

Interestingly, a similar experiment performed with MCF7 cells revealed that collagen mineralization increases rather than decreases MCF7 traction forces, consistent with their increased mesenchymal properties (Fig. 4d and Extended Data Fig. 9). However, the absolute traction forces of MCF7 precultured on collagen were significantly lower than those of MDA-MB231. In contrast, traction forces of MCF7 precultured on mineralized collagen were similar to those of MDA-MB231, possibly suggesting that collagen mineralization leads to an adjustment of cell traction forces favourable for survival in bone. Indeed, the traction forces of BoM-1833, which were isolated from a bone metastasis, were similar to traction forces of MDA-MB231 and MCF7 cultured on mineralized collagen, but did not differ when these cells were cultured on any of the other substrates (Fig. 4d and Extended Data Fig. 9). Collectively, these results suggest that collagen mineralization regulates the phenotype of breast cancer cells by inhibiting cell-mediated collagen remodelling that would otherwise increase growth by activating mechanosignalling.

Mineral content of native bone regulates breast-cancer-cell phenotype

In addition to collagen type I, bone ECM contains other proteins (collectively referred to as non-collagenous proteins or NCPs) that may impact the response of tumour cells to mineral[65]. In addition, the microfabricated collagen substrates described above are not suitable to validate in vitro results in a xenograft setting. To circumvent both limitations, we generated millimetre-sized physiological bone matrices in which we selectively controlled mineral content by adapting previously established protocols[66,67]. We chose to prepare these bone matrices from trabecular bone since it is a preferred site for breast cancer metastasis relative to long bones[68]. First, bone plugs were collected from neonatal bovine femurs and fully decellularized to prepare scaffolds that contained all organic and inorganic matrix components including mineral but were devoid of cells (termed decellularized scaffolds (DC) hereafter). Next, DC scaffolds were demineralized with ethylenediaminetetraacetic acid (EDTA), resulting in decellularized and demineralized (DCDM) scaffolds (Fig. 5a). Adequate decellularization was verified histologically and by DNA assay[69] (Fig. 5b). Demineralization of DCDM was confirmed by nano-computed tomography (nano-CT), BSE-SEM and FT-IR, while SEM, second harmonic generation (SHG) microscopy and histological analysis confirmed that scaffold architecture and collagen fibrillar structure were not affected by the demineralization procedure (Fig. 5c, and Supplementary Figs. 4 and 5). SEM analysis also indicated that the average diameter of collagen and mineralized collagen fibres in these scaffolds was comparable to the fibre diameter in our synthetic substrates, but more variable (Fig. 5d). Moreover, the pXRD patterns of DC scaffolds as well as their mineral to matrix ratio were comparable to physiological bone (and mineralized collagen) (Extended Data Fig. 1; mineralized collagen: ~4; human bone: 3–6)[26], suggesting that the decellularization step had no effect on the mineral phase (Fig. 5e,f). Crystallinity of the HA in the DC scaffolds was also comparable to naïve bone but reduced relative to HA in mineralized collagen or pure HA, a difference that may be explained by the young age of the animals from which the bone was collected (Fig. 5g).

After characterizing the bone scaffolds and confirming by SEM that MDA-MB231 cells adhered to and grew within the 3D scaffolds (Fig. 5h), we asked whether proliferation and stem-like behaviour of breast cancer cells were altered by the different scaffold conditions. DNA analysis identified that cell growth within DC scaffolds was lower than that within DCDM scaffolds, supporting that the presence of mineral reduces breast cancer cell growth in these systems (Fig. 5i). Confocal imaging and flow cytometry of Nanog-GFP MDA-MB231 showed that breast cancer cells increased GFP expression and assumed more stem-like phenotypes when grown within mineral-containing DC scaffolds relative to PS and DCDM scaffolds (Fig. 5j,k). Taken together, these results indicate that the presence of mineral alters breast cancer cell behaviour in physiological bone scaffolds, similar to the synthetic mineralized collagen scaffolds, thus validating the broader significance of mineral to regulating tumour-cell phenotypes.

https://doi.org/10.1038/s41551-023-01077-3

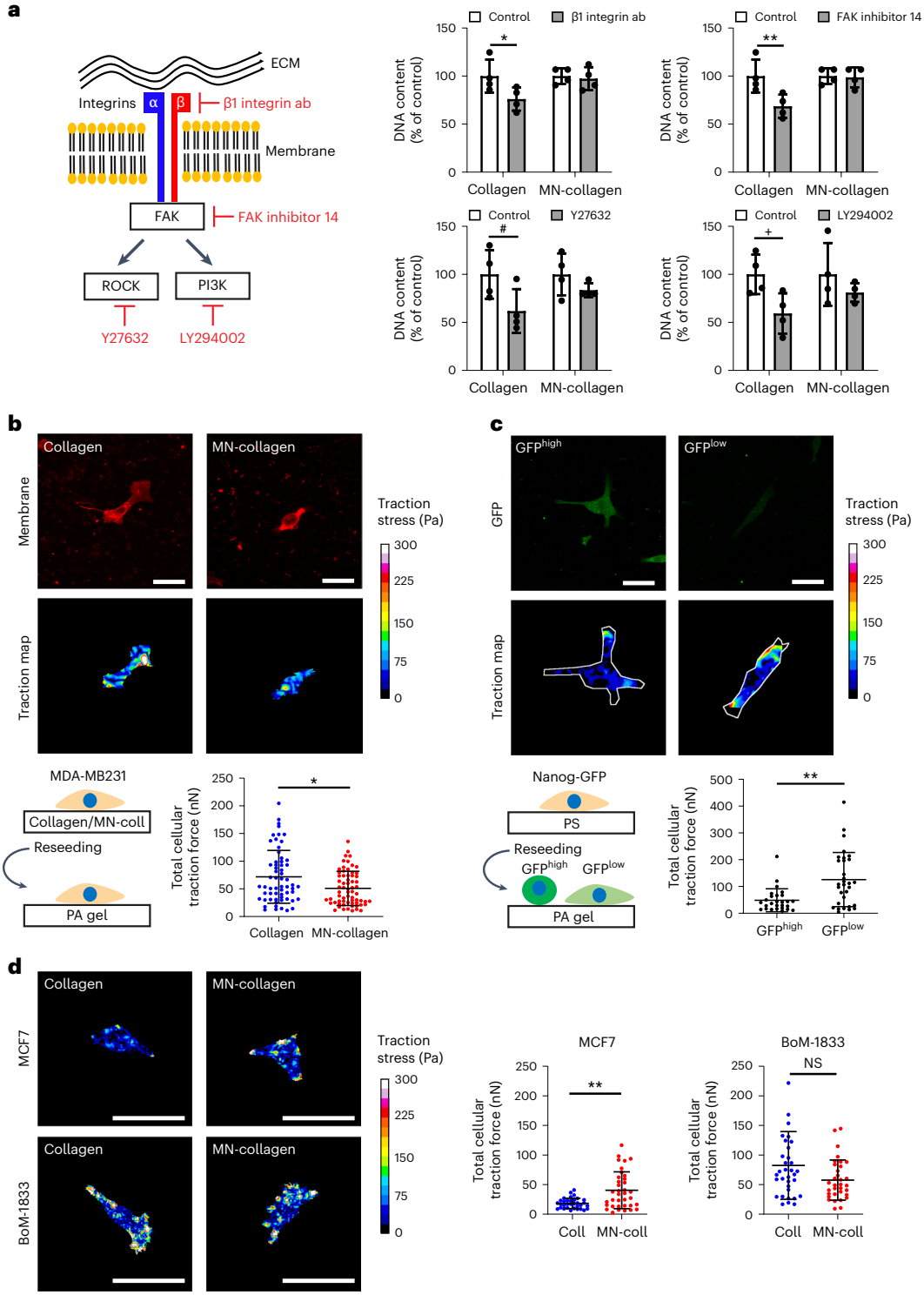

Fig. 4 | Collagen mineralization alters breast cancer cell mechanotransduction. a, Schematic of integrin-mediated mechanosignalling (left) and effect of different mechanosignalling inhibitors (right) on the growth of MDA-MB231 cells cultured on collagen and mineralized collagen ($n = 4$; $^{*}P = 0.0416$; $^{**}P = 0.0075$; $^{\#}P = 0.0438$; $^{+}P = 0.0498$). **b**, Traction force microscopy of MDA-MB231 cells following preculture on collagen and mineralized collagen. Representative images of MemGlow 590-labelled cells (top), traction maps (middle) and corresponding quantification of traction forces (bottom) (at least 61 cells examined from 6 gels; $^{*}P = 0.0123$). Scale bar, 50 µm. **c**, Traction force microscopy of GFP^{high} and GFP^{low} MDA-MB231 cells. Representative fluorescence images (top), traction maps (middle) and corresponding quantification of traction forces (bottom) of Nanog-GFP cells (at least 27 cells examined from 5 gels; $^{**}P = 0.0017$). White lines on traction maps indicate contour of cell. Scale bar, 50 µm. **d**, Traction force microscopy of MCF7 and BoM-1833 cells following preculture on collagen and mineralized collagen. Representative images of traction maps (left) and corresponding quantification of traction forces (right) (at least 33 MCF7 cells examined from 5 gels; $^{**}P = 0.0046$; at least 33 BoM-1833 cells examined from 3 gels). Scale bar, 50 µm. Pseudocolour images in **b**–**d** represent the calculated traction stresses, as described in Methods, limited to the cell boundaries, and colour determined on the basis of magnitude. Data are mean ± s.d. Statistical differences were determined using two-way ANOVA with Sidak's multiple comparisons test for data in **a** and two-tailed Mann–Whitney *U*-test for data in **b**–**d**.

https://doi.org/10.1038/s41551-023-01077-3

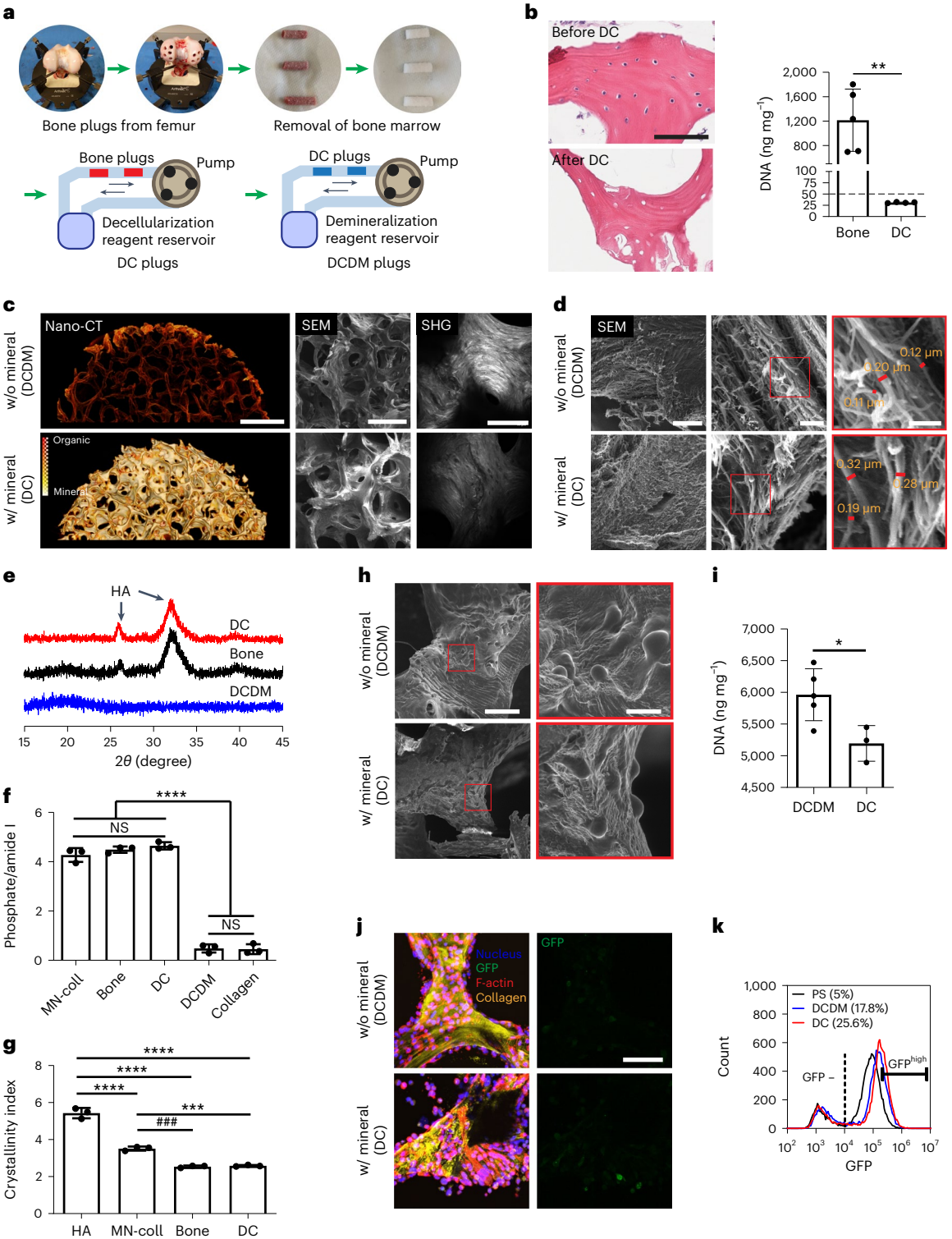

Fig. 5 | Physiological bone scaffolds to test the effect of bone mineral on the stem-like phenotype of MDA-MB231. a, Schematic visualizing the preparation of DC and DCDM bone scaffolds from 1–2 cm long, 6-mm-diameter neonatal bovine femur bone plugs. **b**, H&E staining and DNA quantification of scaffolds after the DC process (bone: $n = 5$, DC: $n = 3$; $^{**}P = 0.0026$). Scale bar, 100 µm. Dashed line indicates target decellularization threshold of 50 ng of DNA per dry mg of scaffold. **c**,**d**, Representative nano-CT, SEM and SHG images (**c**) and SEM and fibre diameter analysis (**d**) of scaffolds after DCDM treatment. Scale bars: 1 mm (nano-CT and SEM), 150 µm (SHG) (**c**); and 10 µm (left), 2 µm (middle) and 1 µm (right) (SEM) (**d**). **e**–**g**, pXRD analysis of mineral phase (**e**) and FT-IR analysis of mineral to matrix ratio (**f**) ($n = 3$; $^{****}P < 0.0001$) and crystallinity index (**g**) ($n = 3$; $^{***}P = 0.0004$; $^{****}P < 0.0001$; $^{###}P = 0.0003$) after the DC and DCDM processes. Commercially available HA served as control. **h**,**i**, SEM images (**h**) and DNA quantification (**i**) of MDA-MB231 cells cultured on the different scaffolds (DCDM: $n = 5$, DC: $n = 3$; $^{*}P = 0.0302$). Scale bar, 50 µm (left) and 10 µm (right). **j**,**k**, Confocal images (**j**) and flow cytometry analysis (**k**) of Nanog-GFP cells cultured on the different scaffolds. Scale bar, 100 µm. Data are mean ± s.d. Statistical differences were determined using two-tailed unpaired *t*-test for data in **b** and **i**, and one-way ANOVA with Tukey's multiple comparisons for data in **f** and **g**.

https://doi.org/10.1038/s41551-023-01077-3

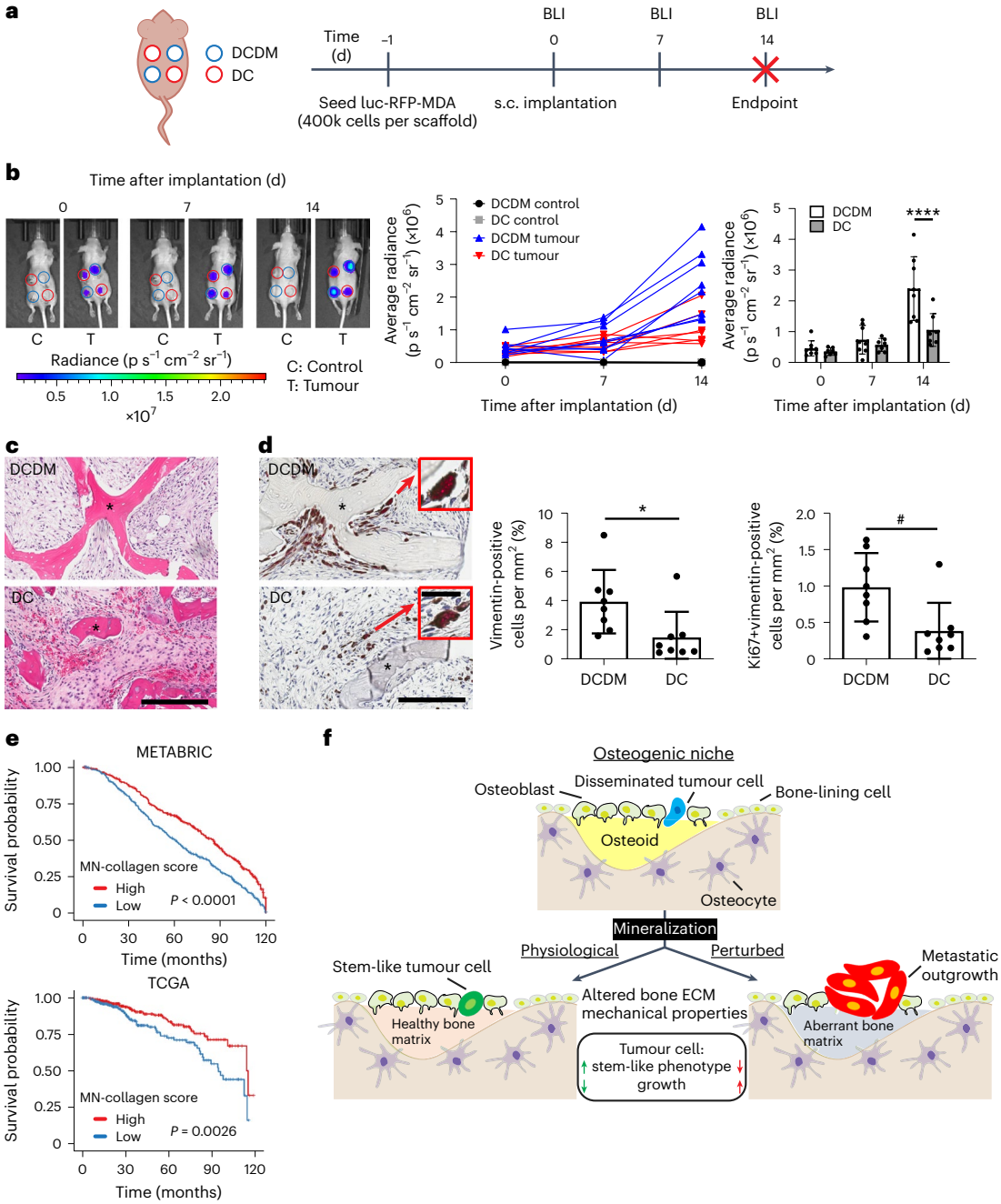

Fig. 6 | Mineralized bone matrix reduces tumour growth in vivo and mineral-induced gene expression signature correlates with improved patient prognosis. a, Time course of xenograft experiment involving implantation of MDA-MB231-seeded DCDM and DC scaffolds into female nude mice. **b**, Representative BLI images and BLI quantification of tumour growth on the different bone scaffolds (DCDM: $n = 8$, DC: $n = 7$; $^{****}P < 0.0001$). Pseudocolour indicates radiance pixel intensity between 1.32×10^6 and 2.72×10^7 p s^{-1} cm^{-2} sr^{-1}. Quantification of BLI images is shown as both line and bar charts to display individual sample change and statistical difference over time. **c**,**d**, Representative H&E images (**c**) and IHC images (left) and analysis of vimentin (middle) and vimentin/Ki67-positive cells (right) (**d**) ($n = 8$; $^{*}P = 0.0265$; $^{\#}P = 0.0144$) in implanted bone scaffolds. Scale bar, 200 µm and 30 µm (inset). Asterisk in images indicates scaffold. **e**, Overall survival of patients with breast cancer scoring high or low for expression of mineral-induced gene signatures (Supplementary Table 2) using the METABRIC and TCGA cohorts. **f**, Proposed relationship between bone ECM and breast cancer-cell phenotype. Our results suggest that mineralization of collagen type I-rich osteoid in osteogenic niches induces stem-like, less-proliferative phenotypes in breast cancer cells. As bone-matrix mineralization changes (such as owing to aging), tumour-cell growth is activated possibly due to bone-matrix-dependent changes in tumour-cell mechanosignalling. Data are mean ± s.d. Statistical differences were determined using two-way ANOVA with Sidak's multiple comparisons test for data in **b** and two-tailed unpaired *t*-test for data in **d**.

Bone mineral affects breast cancer progression in vivo

To test the relevance of bone-matrix mineralization to tumour growth in vivo, decellularized physiological bone matrices with (DC) and without mineral (DCDM) (Fig. 5a) were seeded with luciferase-expressing MDA-MB231s, xenografted into female athymic Nude-*Foxn1*^{nu} mice and then tracked longitudinally by bioluminescence intensity (BLI) imaging (Fig. 6a). Tumour cells interacted with trabecular surfaces of both scaffold types but grew significantly more on matrices devoid of

mineral (Fig. 6b,c). Accordingly, co-immunostaining against human vimentin and Ki67 confirmed that tumours in mineral-containing DC scaffolds contained fewer human tumour cells than their DCDM counterparts and that tumour cells were less proliferative relative to tumour cells growing in DC scaffolds (Fig. 6d). These results imply that mineralized bone matrix not only reduces tumour-cell proliferation in vitro, but also in vivo.

To evaluate the clinical relevance of our findings, we examined whether the gene expression signature induced by culturing tumour cells on mineralized versus control collagen was predictive of overall patient survival and bone metastasis-free survival. Indeed, upregulation of mineral-induced genes was associated with better patient prognosis in the METABRIC and TCGA cohorts, consistent with our in vitro findings that matrix mineralization induces a more latent, less proliferative phenotype (Fig. 6e) and that tumour cells implanted on DCDM scaffolds grew more than their counterparts implanted on DC scaffolds. Analysis of cancer subtypes additionally showed that patients with luminal breast cancer whose tumours primarily metastasize to bone benefitted from upregulation of the mineral-induced gene signature (Supplementary Table 2), whereas patients with basal breast cancer whose cancers preferentially metastasize to visceral organs did not (Extended Data Fig. 10a)[70]. Using two published breast cancer cohorts with clinical data (Study ID: GEO2603, GSE2034), we further validated that patients whose tumours scored high for our mineralized collagen gene signature had improved bone-metastasis-free survival relative to patients whose tumours scored low for this signature (Extended Data Fig. 10b). While this analysis used primary tumour specimens rather than specimens collected from bone metastatic tumours, these results suggest that gene expression profiles induced by mineralized bone matrix correlate with increased patient survival, possibly by selecting for less proliferative phenotypes. More broadly, these results indicate that bone matrix is a critical factor in regulating breast cancer cell fate.

Discussion

Disseminating tumour cells target osteogenic niches within the skeleton[9,10], but the role of collagen type I mineralization (a hallmark of bone formation) in regulating the phenotype of breast cancer has been unexplored. Our results suggest that physiological collagen mineralization induces a less proliferative, more stem-like phenotype in breast cancer cells, whereas perturbed mineralization activates tumour cells to proliferate and form larger tumours (Fig. 6f). These findings could help explain why patients with breast cancer with decreased bone mineral density have a higher risk of developing bone metastasis[12,27].

Although the ECM is known to regulate various aspects of breast cancer including metastasis[71,72], its role in bone metastasis is less clear, as studies on the skeleton are hindered by limited imaging modalities and the difficulty of analysing cells in this context. In vitro models can circumvent some of these limitations by allowing control over the material properties of bone ECM. Here we used biofunctional material systems incorporating the basic building blocks of native bone ECM, HA-reinforced collagen fibrils[18,33]. With these models, we were able to mimic the defining material properties of bone ECM across multiple length scales, including the bone's hierarchical structure, ultrastructural arrangement, mineral to matrix ratio and mineral crystallinity. Leveraging these models, we found that collagen mineralization suppresses cancer-cell proliferation in vitro and tumour growth in vivo, and that mineral-induced changes in tumour stem-like properties may play a role in this process. These results suggest that osteogenic niches may induce quiescence in breast cancer cells owing in part to collagen mineralization, giving new context to previous results showing that tumour cells assume a more stem-like phenotype following bone colonization[54].

Although the mechanical properties of the matrix are widely accepted to affect tumourigenesis, the effect of bone-matrix mineralization on tumour-cell mechanosignalling is poorly understood, owing in part to a lack of model systems that mimic the viscoelastic properties of bone more appropriately than the linearly elastic substrates that are routinely used for mechanosignalling studies. Collagen type I, the primary organic bone-matrix component, exhibits nonlinear elasticity and viscoelasticity[73]. Both properties can affect cell behaviour[21] but are impacted by mineralization[19]. More specifically, tumour cells can activate and reinforce mechanosignalling by strain-stiffening collagen[41], a process that is reduced by collagen mineralization as shown here. On the other hand, stress relaxation occurs more slowly in mineralized collagen than in collagen[20]. Our data suggest that these changes have functional consequences as cancer cells adjust their traction forces following interactions with mineralized versus non-mineralized collagen. In MDA-MB231, these variations in traction forces manifested in a lack of response to pharmacological inhibitors of key nodes of mechanotransduction and correlated with reduced traction forces in more stem-like GFP^{high} versus GFP^{low} cells. Importantly, this correlation extended to an induction of phenotypic changes including the upregulation of stem-cell markers and functions, reduced cell proliferation and increased anchorage-independent survival.

Our findings contradict the conventional assumption that bone stimulates malignancy by increasing mechanosignalling owing to its increased rigidity and underline the importance of choosing the correct material systems for mechanistic studies of tumour–ECM interactions. Indeed, our results corroborate preclinical and clinical evidence indicating that reduced bone mineral density (for example, owing to vitamin D deficiency) correlates with increased risk and outgrowth of bone metastases[15,16,31]. Future studies will need to elucidate how mineralization-dependent changes in tumour-cell phenotype affect other signalling mechanisms. For example, tumour cells can control entry into (and exit from) dormancy by depositing and responding to their own matrix, including fibronectin[64,74]; and altered cell–ECM interactions, in turn, can regulate cellular responses to soluble factors[64]. The fibronectin-binding integrins $\alpha_5\beta_1$ and $\alpha_v\beta_3$, for example, affect transforming growth factor-β signalling via receptor cross-talk[75,76], a process that has been shown to modulate bone metastatic progression[13,77]. Hence, future work should explore how interactions with mineralized collagen affect tumour-cell deposition of fibronectin and, consequently, the expression of known dormancy markers such as NR2F1, which can regulate tumour-cell stemness via Sox2 and Nanog[78]. The influence of other nanoscale changes caused by mineralization, such as altered surface topography or porosity, should also be considered.

Although the focus of this study was on tumour cells, many other cell types residing in the skeleton can equally respond to bone-matrix changes (such as endothelial cells, mesenchymal stromal cells, osteoblasts, osteocytes and immune cells)[9,13,79,80]; and, vice versa, they may alter the bone matrix in response to tumour-cell-secreted systemic or paracrine signals. Accordingly, bone-matrix mineralization by osteoblasts correlated with decreased tumour-cell growth in our experiments, whereas the inhibition of osteogenic differentiation and thus matrix mineralization caused an opposite effect. Although these data were supportive of our overall conclusion, we cannot exclude matrix-independent effects. For example, mineralizing mature osteoblasts secrete factors (such as transforming growth factor β2 or bone morphogenetic proteins 4 and 7) that can induce tumour-cell quiescence independently of the matrix[81], a possibility that should be tested with appropriate control experiments. Fluctuations in nutrient and oxygen supply or in other metabolic constraints could further affect these responses. Future studies will need to increase the complexity of the described culture models to better understand how matrix mineralization impacts the early stages of bone metastasis in multivariate settings.

Although we have validated the in vivo relevance of our findings with animal studies and with computational analysis of patient data, the model systems described herein have some limitations. For example, they did not consider bone-resident cells, and the decellularized bone scaffolds were derived from neonatal bovine bone.

The biomechanical properties of human bone and collagen are conserved between species, but it is likely that additional parameters influence bone-matrix properties and thus cancer-cell response to mineralization. For example, age, gender, lifestyle and previous treatment with chemotherapy are known regulators of the material properties and health of bone[23,24,28,49,82]. Future studies using bone specimens collected from patients will help evaluate these connections and could be combined with matched bone-resident cells and organoid cultures to directly test patient-specific responses to bone-matrix properties. Furthermore, bone mineralization is a dynamic process and it is possible that tumour-cell responses are dependent on the timescales at which this process occurs. The mineralized substrates used here were prefabricated before seeding cells, but it is also possible to mineralize collagen in situ[80]. Finally, the flank implantation model we used allowed for precise control of bone-matrix mineral content independently of other parameters, which is not readily possible in the skeleton itself. Biomaterial scaffolds can influence tumour growth and metastasis by altering the recruitment of immune cells and other stromal cells[83,84]; and whereas we observed infiltration by resident cells, the mineral-induced less proliferative tumour-cell phenotype was maintained. How the phenotype of recruited cells may differ in response to the mineral content of the matrix and how such changes regulate tumour-cell phenotype will need to be considered in future work.

In conclusion, our findings suggest that bone-matrix changes are not only a collateral consequence of osteolytic degradation during late-stage metastasis but may also occur in osteogenic niches, with potential effects on the early-stage development of bone metastases. The finding that bone-matrix mineral content inhibits breast-cancer growth motivates the clinical use of methods to increase or maintain physiological bone-matrix mineralization, for example, by therapies that promote bone formation in settings of mechanical loading or exercise. Bisphosphonates are an alternative strategy to maintain bone mineral density and are routinely used as adjuvant therapy for patients with breast cancer to reduce skeletal-related events and hypercalcemia. However, these drugs are only partially effective in preventing bone metastasis[85,86]. As bisphosphonates primarily prevent bone resorption rather than encourage new bone formation and thus matrix mineralization, our results could help explain the limited success of bisphosphonates in prevention settings. Collectively, our results motivate a more wholistic approach to modelling bone ECM in future studies of bone metastasis and could yield insights that advance treatment options for patients with breast cancer and advanced disease.

Methods

Fabrication of mineralized collagen

Mineralized collagen substrates for cell culture were fabricated using an adapted PILP process (Fig. 1c) as previously described[20,37]. Briefly, PDMS (Dow Corning) microwells (diameter: 4 mm, height: 250 µm) were prepared on a larger circular 8 mm PDMS base that enables face-down flotation of the devices necessary for intrafibrillar mineralization, rather than sedimentation of mineral, as further described below. Before casting collagen, the inner surface of the microwell was treated with oxygen plasma, 1% polyethyleneimine (PEI) (Sigma-Aldrich) and 0.1% glutaraldehyde (GA) (Thermo Fisher) to allow for subsequent covalent binding of pH-adjusted rat tail collagen type I (Corning) (1.5 mg ml^{-1}). Mineralization was accomplished using a solution of 62.5 µg ml^{-1} PAA (MW = 27 kDa, Alamanda Polymers), 1.67 mM $CaCl_2$ (Thermo Fisher) and 1 mM $(NH_4)_2HPO_4$ (Sigma-Aldrich) in 0.85× phosphate buffered saline (PBS). To prevent precipitation of mineral on top rather than within collagen fibrils, substrates were incubated in the mineralization solution upside down using a humidified chamber for 1 d at 37 °C. Collagen control substrates were fabricated similarly but immersed in PBS solution rather than mineralization solution. To adjust mineral content via controlled dissolution, fully mineralized collagen was incubated in 20 mM HEPES buffer (pH 7.4) at ambient temperature for up to 6 d, changing HEPES buffer every 12 h.

Characterization of mineralized collagen

For characterization, collagen substrates were prepared on PEI/GA-treated 8-mm-diameter glass coverslips adhered to a PDMS base. SEM (Mira3 LM, Tescan) visualized fibre morphology and confirmed mineral formation using secondary electron (SEM) and BSE imaging modes. To this end, samples were dehydrated with a series of ethanol solutions and hexamethyldisiloxane and then carbon coated (Desk II, Denton Vacuum). Changes in collagen fibril diameter were analysed using the diameterJ function in ImageJ (NIH). Presence of mineral was detected by pseudocolour processing of BSE images using MATLAB (MathWorks). Mineral formation was also confirmed by FT-IR spectrometry (Hyperion 2000/Tensor 27, Bruker). Samples were pelleted with potassium bromide (Thermo Fisher) and scanned in the range of 400–2,000 cm^{-1}. Mineral to matrix ratio was determined by calculating the ratio of phosphate peak area (907–1,183 cm^{-1}) and collagen amide I peak area (1,580–1,727 cm^{-1}) after correcting the FT-IR spectra base line using spectroscopy software (OPUS, Bruker). The crystallinity index of mineral (CI = $(A_{567} + A_{603})/A_{590}$, where A_x is the absorbance at wave number x) was determined using phosphate band splitting (Extended Data Figs. 1 and 7c). The phase of the formed mineral was determined using a powder X-ray diffractometer (D8 advance ECO powder diffractometer, Bruker). Dried samples were mounted on a polymethyl methacrylate specimen holder and scanned in the range $2\theta = 15–45°$, with a step size of 0.0195° and Cu Ka radiation ($\lambda = 1.54$ Å). Mechanical properties of substrates were measured using a rheometer (DHR3, TA instruments) with 20 mm top- and bottom-plate geometry, and built-temperature and distance calibration. Collagen substrates were first cast and mineralized within a PDMS ring mounted onto 20 mm PEI/GA-coated coverslips. For rheological measurements, the PDMS ring was removed and the coverslips with the substrates were attached to the bottom plate. Subsequently, a PEI/GA-coated coverslip was attached to the top plate and the top plate was lowered onto the sample at 500 µm distance between plates. In this configuration, the sample was incubated for 15 min at 37 °C in the presence of PBS before rheological measurements. For the storage (G') and loss (G'') moduli, time sweeps were performed at 1% strain with an oscillation frequency of 2π rad s^{-1}. Strain stiffening was measured using strain-sweep experiments with an oscillation frequency of 1 rad s^{-1}. Stress relaxation was measured using time-sweep experiments after applying 40% strain with a rise time of 0.01 s.

Cell culture and phenotypic characterization

MDA-MB231 breast cancer cells (ATCC), MDA-MB231 expressing a Nanog-GFP reporter[55] (Nanog-GFP), bone metastatic BoM1-2287 and BoM-1833 (kindly provided by Joan Massague) and MCF7 (ATCC) were routinely cultured in Minimum Essential Medium α (α-MEM) (Thermo Fisher) supplemented with 10% (v/v) fetal bovine serum (FBS) (Atlanta Biologicals) and 1% penicillin/streptomycin (P/S) (Thermo Fisher). Substrate-dependent differences in cell adhesion and growth were determined by fluorescence analysis of DNA content with the QuantiFluor dsDNA kit (Promega) after 5 h and 7 d of culture, respectively. For analysis of the fibronectin effect on cell growth, substrates were incubated with PBS solution containing various concentrations of human plasma fibronectin (Thermo Fisher) for 2 h. Before cell seeding, fibronectin-adhered substrates were transferred to cell culture media containing 10% FBS and 1% P/S. For analysis of cell morphology after 5 h of adhesion, cells were fixed with 10% formaldehyde and stained with DAPI (Invitrogen) and Alexa Fluor 568 phalloidin (Thermo Fisher). Confocal images (710 LSM, Zeiss) were captured with a ×40 water immersion objective at 2 µm step size. Cell morphology was analysed using randomly selected images per sample ($n = 4$). At least 200 cells per condition were analysed using built-in functions of ImageJ for

projected cell area and aspect ratio. Collagen structure was imaged in reflectance mode using a 488 nm laser. Cell proliferation was assessed after 7 d using Ki67 staining. Fixed samples were blocked with 1% BSA in PBS, stained using rabbit anti-human Ki67 monoclonal antibody (Cell Signaling Technologies), detected with goat anti-rabbit Alexa Fluor 568 secondary antibody (Thermo Fischber) and counterstained with DAPI. Ki67 levels per cell were analysed from at least four randomly selected areas per sample ($n = 4$) and quantified using ImageJ. Cell proliferation was also measured after 4 d using a BrdU staining kit (Life Biotechnologies) according to manufacturer instructions. Images from six randomly selected areas per sample ($n = 3$) were captured with an epifluorescence microscope and BrdU-positive cells were quantified using ImageJ.

hMSC experiments

hMSCs (RoosterBio) were routinely cultured in RoosterNourish-MSC media. hMSCs were seeded on collagen-coated 18 mm glass coverslips. Tumour conditioned media were generated by culturing MDA-MB231 breast cancer cells (ATCC) until 90% confluency in Dulbecco's Modified Eagle Medium (DMEM)/10%FBS/1%P/S, then media were replaced with serum-free media (DMEM, 1% P/S) for 24 h. Conditioned media were collected and concentrated 10-fold in an Amicon centrifugal filter unit (MWCO 3k Da, EMD Millipore) and subsequently diluted 5-fold with hMSC media. hMSCs were treated with tumour conditioned media, osteogenic induction media (50 µM ascorbic acid, 0.1 µM dexamethasone, 10 mM β-glycerophosphate) and/or control DMEM media every 2–3 d. After 21 d, hMSC mineral deposition was assessed via Alizarin Red S staining. Samples were fixed with 4% PFA for 15 min and incubated with 40 mM Alizarin Red S (VWR) for 30 min, followed by washing with distilled water. To assess hMSC fibronectin deposition, fixed samples were blocked with 1% BSA in PBS, stained using mouse anti-human fibronectin monoclonal antibody (Sigma-Aldrich) and detected with goat anti-mouse Alexa Fluor 488 secondary antibody (Thermo Fisher). Cells were counterstained with DAPI (Invitrogen).

To assess changes in cancer cell proliferation after hMSC pretreatment, MDA-MB231 cells were labelled with CellTracker Orange CMRA dye (Invitrogen) according to manufacturer instructions and seeded onto hMSC cultures that were treated for 21 d. After 2 d of culture, samples were fixed with 4% PFA and counterstained with DAPI (Invitrogen). Confocal images (710 LSM, Zeiss) were captured with a ×10 air objective from 5 randomly selected areas per sample ($n = 3$) and tumour-cell number (per field of view) was quantified using ImageJ.

Analysis of stem-like tumour-cell phenotype

To validate the Nanog-GFP reporter cell line, cells were sorted into GFP^{high} and GFP^{low} populations using FACS. Sorted cells were lysed with RIPA buffer containing protease and phosphatase inhibitors (Thermo Fisher) and 1 mM phenylmethylsulfonyl fluoride (Calbiochem). All samples with equal amounts of protein were loaded on gels and separated by reducing SDS–PAGE and transferred to PVDF membranes (Bio-Rad). Membranes were blocked with 5% milk powder and incubated with rabbit anti-human Sox2 (Sigma-Aldrich), rabbit anti-human Oct4 (Millipore) and rabbit anti-human HSP90 (Santa Cruz) overnight. Primary antibodies were detected by a horseradish peroxidase-conjugated anti-rabbit antibody using an ECL kit (Thermo Fisher) and imaged using a ChemiDoc TM Touch imaging system (Bio-Rad). Captured images were analysed with Image Lab software (Bio-Rad). The experiment was conducted twice. For analysis of the matrix effect on GFP expression, Nanog-GFP cells were cultured on the different matrices and GFP levels per cell were analysed from confocal images using the threshold tool in ImageJ. For flow cytometry, Nanog-GFP cells cultured on tissue culture PS were trypsinized, while cells cultured on collagen and mineralized collagen were isolated using collagenase type I (1 mg ml^{-1} in PBS, Worthington Biochemical). Suspended cells were passed through a 40 µm cell strainer, centrifuged and resuspended in flow cytometry buffer containing propidium iodide (Invitrogen) for subsequent flow cytometry (BD Accuri C6 Plus, BD biosciences). ALDH activity of cells was measured using an ALDEFLUOR kit (STEMCELLTechnologies) according to manufacturer instructions. Cells were gated by forward scatter (FSC) and side scatter, then FSC-A and FSC-H signals were used for doublet exclusion. Live cells selected on the basis of propidium iodide signals were used to identify cell populations expressing GFP from Nanog-GFP and ALDH from MDA-MB231. To analyse colony formation in soft agar, cells isolated from the different matrices (5×10^4 cells) were suspended in a solution of 0.3% noble agar in DMEM with 10% FBS and 1% P/S and then plated on a layer of 0.5% noble agar in 6-well plates. After gelation, the plate was cultured in DMEM with 10% FBS and 1% P/S. After 21 d, cultures were incubated in media containing nitroblue tetrazolium (Biotium) overnight. Sphere formation was visualized using a ChemiDoc Touch imaging system (Bio-Rad) and analysed using the ImageJ particle analysis tool. Colonies over 100 µm in diameter were counted and measured for colony diameter distribution. For analysis of stemness and E-cadherin expression of MCF7 cells, MCF7 cells were cultured on the different matrices for 7 d. MCF7 cells were assessed for the $CD44^+/CD24^-$ stem-like fraction via flow cytometry using a BD Accuri C6 Plus Analyzer. Following trypsinization, cells were resuspended in FACS buffer (PBS containing 2.5% FBS, 2 mM EDTA) at 10×10^6 cells per ml, followed by incubation with antibodies against human CD44 (APC-conjugated, Clone G44-26, 1:5, BD Biosciences) and CD24 (PE-Cy7-conjugated, Clone ML5, 1:20, BD Biosciences). Gates were created in FCS Express and determined using the isotype controls mouse anti-IgG2b κ (APC-conjugated, Clone 27–35, 1:5, BD Biosciences) and mouse anti-IgG2a κ (PE-Cy7-conjugated, Clone G155-178, 1:20, BD Biosciences). E-cadherin expression was analysed from confocal images. Cells were stained using mouse anti-human E-cadherin (BD Biosciences) and detected with goat anti-mouse Alexa Fluor 568 secondary antibody (Thermo Fisher). E-cadherin levels per cell were analysed from 4 randomly selected areas per sample ($n = 3$) and quantified using ImageJ.

Analysis of mechanosignalling-mediated changes in cell growth

For analysis of mineralization-dependent changes in mechanosignalling, MDA-MB231 cells were cultured on PS, collagen and mineralized collagen in the presence and absence of a function-blocking β1 integrin antibody (2 µg ml^{-1}, Millipore) or pharmacological inhibitors of FAK (FAK inhibitor 14, 5 µM, Tocris), ROCK (Y27632, 25 µM, Tocris) or PI3K (LY294002, 10 µM, Tocris) for 4 d. Subsequently, cell growth was analysed by measuring DNA content as described above.

Analysis of cell traction forces

Polyacrylamide gels were prepared with a Young's modulus of either 2.7 kPa for Nanog-GFP and 5 kPa for MDA-MB231 cells as previously described[87]. Briefly, 35 mm glass-bottom dishes (VWR) were cleaned with 0.1 N NaOH, followed by sequential surface treatment with 3-aminopropyl-trimethylsilane and 0.5% (v/v) GA in PBS. Dishes were washed with distilled water and allowed to air dry. Prepolymer solutions for gels were prepared by combining 40% acrylamide, 2% bisacrylamide, PBS and 0.2 µm fluorescent beads (Thermo Fisher). Gels (2.7 kPa and 5 kPa) were prepared using 7.5%/0.035% and 7.5%/0.06% of acrylamide/bisacrylamide, respectively. Polymerization was initiated through the addition of ammonium persulfate and *N,N,N,N*-tetramethyl ethylenediamine. Droplets of the polymer solution were placed between activated dishes and a Sigmacote-treated 8 mm coverslip (Sigma-Aldrich) and allowed to polymerize. Polyacrylamide gels were functionalized with rat tail type I collagen (0.03 mg ml^{-1}) using an N6 succinimide ester crosslinker solution as previously described[88]. Gels were washed with PBS and cell media before cell seeding at 1×10^3 cells per cm^2.

Confocal microscopy (810 and 880 LSM, Zeiss) was used to image Nanog-GFP or MemGlow 590 (20 nM, Cytoskeleton) labelled

MDA-MB231 cells using either ×63 or ×40 1.2NA C-Apochromat objectives. Cells were lysed by adding 2% sodium dodecyl-sulfate (SDS) to the dishes (final concentration of 1% SDS) and gels allowed to relax for 2 min. Images of the relaxed gels were then acquired at the same positions. Images of beads were sharpened and stage drift corrected using ImageJ, and bead displacements and corresponding forces calculated using previously developed software and custom MATLAB scripts[89]. Cellular traction forces were calculated using the Fourier transform traction cytometry method with a regularization parameter (λ) of 1×10^{-9}. For MDA-MB231, MCF7 and the bone tropic MDA-MB231 subclone BoM-1833 traction forces of at least 10 cells were analysed per gel for a minimum of 2 gels per condition. For Nanog-GFP, traction forces of at least 25 cells per condition were analysed from 5 gels. Pairwise comparisons of total cellular traction forces were conducted using either a Mann–Whitney *U*-test or a Kruskal–Wallis test with Dunn's multiple comparison correction when more than two conditions were being compared. For cellular traction forces when cells were precultured on different substrates, outliers were identified using the robust regression followed by outlier identification method with a *Q* value of 1%.

RNA-sequencing and data analysis

Cells were collected using collagenase after 7 d of culture and RNA was isolated from each condition using an RNA isolation kit (Qiagen) according to manufacturer protocols ($n = 4$). Illumina TruSeq RNA stranded kit (Illumina) was used for library preparation, and samples were sequenced as 1 × 86 bp single-end reads on a NextSeq500 system (Illumina), yielding on average 42 M reads per sample. Reads were then trimmed using Trim Galore (v.0.4.4; https://www.bioinformatics.babraham.ac.uk/projects/trim_galore/) and aligned to the human reference genome GRCh38 (ENSEMBL) using STAR (v.2.6.0a)[90]. Reads of genomic features were counted using featureCounts[91] and differential gene expression determined using DESeq2 (ref. 92). Differentially expressed genes were defined as those with a $\log_2$(fold change) > |1| and an adjusted *P* value (P_{adj}) < 0.05. For GSEA, a ranked list was generated by taking the sign of the fold change multiplied by the $-\log_{10}$ of P_{adj}. The list was inputted to the GSEA Java applet (http://software.broadinstitute.org/gsea/index.jsp) using gene ontology (GO) biological processes gene sets from MSigDB v.6.2. Gene sets were considered significantly enriched with a *P* value and false discovery rate (FDR) value less than 0.05.

The relevance of gene expression changes induced by mineralized collagen to human breast cancer samples was computed using publicly available TCGA and METABRIC datasets. The 98-gene mineralized collagen gene signature was defined as transcripts with a $\log_2$(fold change) ≥ 1 and a $P_{adj} \leq 0.05$. The transcriptional score based on supervised gene signature was computed across all samples using the single-sample GSEA (SSGSEA) method from the gsva package. SSGSEA scores were used for clinical correlations with survival. In the TCGA and METABRIC cohorts, sorted signature scores in the upper and lower tertiles were classified as high and low transcriptional signatures, respectively. Kaplan–Meier survival analysis was then performed with coxph regression using the 'survival' package in R to associate transcriptional signature score with overall survival as primary outcome.

To assess association of our mineralized collagen gene signature with bone-metastasis-free survival, two published breast cancer cohorts with clinical data (Study ID: GEO2603, GSE2034) were used. ComBat function from the sva library was used to batch correct the cohorts before the analysis. As the used published data were generated by microarray, which analyses predefined transcripts/genes rather than the whole transcriptome, we were able to map only a subset of our RNA-seq-derived 98 gene signatures to the microarray probe (GLP96) set in this cohort. Despite this technological limitation with the dataset, we were able to use 55 out of the 98 genes that mapped to the available probe set. This subset of 55 genes was used as the mineralized collagen gene signature to compute the transcriptional signature score using SSGSEA as above. Across the cohorts, sorted signature scores in the upper and lower quartiles were classified as high and low transcriptional signatures, respectively. Kaplan–Meier survival analysis was then performed with coxph regression using the 'survival' package in R to associate transcriptional signature score with bone-metastasis-free survival.

Preparation and characterization of bone scaffolds

Trabecular bone biopsies were extracted from 1–3-day-old neonatal bovine distal femurs as previously described[66]. After rinsing with a high velocity stream of deionized water to remove marrow and debris, biopsies were sectioned into cylindrical scaffolds (6 mm diameter and 1 mm thickness). Scaffolds were incubated in an extraction buffer of 20 mM NaOH and 0.5% Triton X-100 in PBS at 37 °C to remove cells and cellular debris, then incubated in 20 U ml^{-1} DNase I to remove any latent DNA fragments (DC scaffolds). Bone mineral was removed from DC scaffolds via an overnight incubation in 9.5% EDTA (DCDM scaffolds). All scaffolds were then washed 5 times with PBS to clear any residual material. Removal of cellular components was confirmed by hematoxylin and eosin (H&E) staining as well as DNA quantification. To confirm demineralization, scaffolds were scanned on a high-resolution 3D X-ray microscope (Xradia Zeiss Versa XRM-520, Zeiss) at 60 kV/5 W, with exposures of 1.5 s each at a resolution of 3.53 µm per pixel and false-coloured on the basis of the attenuation coefficient (Avizo, Thermo Fisher). To assess collagen content, Masson's trichrome staining was performed on formalin-fixed paraffin-embedded sections according to standard protocols. Trabecular structure and collagen fibrillar structure in DC and DCDM scaffolds were determined by SEM, while the presence of mineral was determined by BSE. The collagen microstructure of DC and DCDM scaffolds was also measured by SHG microscopy. XRD and FT-IR spectra were used to characterize mineral properties of scaffolds as described above. For detection of cell growth, MDA-MB231 cells were imaged by SEM and quantified by fluorescence analysis of DNA content with the QuantiFluor dsDNA kit (Promega). For detection of stem-like properties of cells in scaffolds, GFP expression of Nanog-GFP was imaged by confocal microscopy and quantified using flow cytometry.

Animal studies

Mouse studies were performed in accordance with Cornell University's animal care guidelines and approved by Cornell University's Institutional Animal Care and Use Committee (protocol 2011-0006). For detection of disseminated tumour cells relative to mineralizing bone surfaces, MDA-MB231 cells were labelled with fluorescent silica nanoparticles containing positively charged Cy5 dye (Cy5(+)-SNPs) as previously described[35]. Briefly, cells were labelled with 1 µM Cy5(+)-SNPs and resuspended in ice-cold PBS for mouse injections. Female athymic nude-*Foxn1*^{nu} (Envigo) mice were injected intraperitoneally with calcein (15 mg kg^{-1}, pH 7.4 in PBS) at 5–6 weeks of age. One day later, labelled cells (1×10^5 cells in 100 µl PBS) were injected into the left cardiac ventricle using ultrasound guidance (Vevo VisualSonics 2100, FUJIFILM VisualSonics). Injection into the systemic circulation was verified by bioluminescence imaging (IVIS Spectrum, Perkin Elmer). Tibiae were collected after 2 d. Immediately following collection, tibiae were fixed in ice-cold 4% paraformaldehyde (pH 7.4 in PBS) for 16 h. To detect tumour cells labelled with Cy5(+)-SNPs, tibiae were optically cleared using ethyl cinnamate following dehydration in a graded ethanol series[93]. Samples were imaged in ethyl cinnamate using a light-sheet microscope (LaVision BioTec), using the 488 nm laser to detect calcein and the 640 nm laser to detect Cy5(+)-SNPs. Arivis Vision4D (Arivis) and ImageJ were used to process light-sheet microscopy images.

For in vivo tumour formation, luciferase-expressing MDA-MB231 were seeded on bovine bone scaffolds (6 mm diameter and 1 mm thickness) in α-MEM with 10% FBS and 1% P/S (4×10^5 cells per scaffold) and cultured at 37 °C in a 5% CO_2 incubator for 24 h before implantation. Cell-laden scaffolds (DC versus DCDM) were implanted subcutaneously

(s.c.) into 6–8-week-old female athymic nude-*Foxn1*^{nu} mice (Envigo). Two scaffolds per condition were implanted into each mouse (that is, 4 scaffolds per mouse; $n = 4$ mice; 8 scaffolds per condition). Bioluminescence images were taken once weekly 5 min following injection of D-luciferin (Gold Biotechnology) using an in vivo imaging system (IVIS Spectrum, Perkin Elmer). Outliers were determined using a Grubb's test with a significance level of alpha = 0.0001. Explanted scaffolds were fixed with ice-cold 4% paraformaldehyde and decalcified with 10% EDTA. Paraffin sections were used for H&E staining as well as sequential double-immuno-staining with rabbit anti-human Ki67 (Cell Signaling Technologies) and rabbit anti-human vimentin (Thermo Fisher). First, Ki67 antibody was detected with an alkaline phosphatase-conjugated horse anti-rabbit antibody to stain red following incubation with alkaline phosphatase substrate (Vector Laboratories). After blocking Ki67-stained samples with horse serum, human vimentin antibody was detected with an horseradish peroxidase-conjugated horse anti-rabbit antibody and diaminobenzidine to produce a brown colour (Thermo Fisher). All sections were counterstained with Mayer's haematoxylin (Thermo Fisher) and imaged using a ScanScope slide scanner (Aperio CS2, Leica Biosystems) with a ×40 objective. To quantify Ki67 and vimentin immunoreactivity, images of all immunohistochemistry (IHC)-stained sections were uploaded to QuPath v.0.2.0 (ref. 94) and manually annotated to include cells and exclude trabeculae, lipid deposits and extracellular debris. A QuPath script was written to quantify the total number of cells, total section area and number of cells positive for vimentin and Ki67 per section area. Each data point represents the percentage of positive cells per mm^2 as identified for the cross-sectional area of 1 implant; 8 implants were analysed per condition.

Statistics and reproducibility

Unless otherwise indicated, results are presented as the mean and standard deviation of at least 3 independent replicates per condition using GraphPad Prism 9. Statistical differences were determined using Student's unpaired *t*-test for two group comparisons, one-way analysis of variance (ANOVA) followed by Tukey's post test for multiple group comparisons and two-way ANOVA with Sidak's multiple comparison for multiple factors, unless otherwise mentioned. Two-tailed test with $P < 0.05$ were considered significant in all cases. Statistical considerations for analysis of cell traction forces and tumour growth in vivo are specified in the respective sections above.

Reporting summary

Further information on research design is available in the Nature Portfolio Reporting Summary linked to this article.

Data availability

The main data supporting the results in this study are available within the paper and its Supplementary Information. All RNA-sequencing data generated in this study are available in the NIH Gene Expression Omnibus via the accession number GSE229094. Survival analysis was conducted using publicly available datasets (Study ID: GEO2603, GSE2034). Source data for the figures are provided with this paper.

Code availability

The QuPath script used for immunochemistry analysis is available as Supplementary Information.

References

1. Hess, K. R. et al. Metastatic patterns in adenocarcinoma. *Cancer* **106**, 1624–1633 (2006).
2. Kuchuk, I. et al. Incidence, consequences and treatment of bone metastases in breast cancer patients—experience from a single cancer centre. *J. Bone Oncol.* **2**, 137–144 (2013).
3. Braun, S. et al. A pooled analysis of bone marrow micrometastasis in breast cancer. *N. Engl. J. Med.* **353**, 793–802 (2005).
4. Guise, T. A. The vicious cycle of bone metastases. *J. Musculoskelet. Neuronal Interact.* **2**, 570–572 (2002).
5. Lawson, M. A. et al. Osteoclasts control reactivation of dormant myeloma cells by remodelling the endosteal niche. *Nat. Commun.* **6**, 8983 (2015).
6. Hüsemann, Y. et al. Systemic spread is an early step in breast cancer. *Cancer Cell* **13**, 58–68 (2008).
7. Risson, E., Nobre, A. R., Maguer-Satta, V. & Aguirre-Ghiso, J. A. The current paradigm and challenges ahead for the dormancy of disseminated tumor cells. *Nat. Cancer* **1**, 672–680 (2020).
8. Phan, T. G. & Croucher, P. I. The dormant cancer cell life cycle. *Nat. Rev. Cancer* **20**, 398–411 (2020).
9. Croucher, P. I., McDonald, M. M. & Martin, T. J. Bone metastasis: the importance of the neighbourhood. *Nat. Rev. Cancer* **16**, 373–386 (2016).
10. Wang, H. et al. The osteogenic niche promotes early-stage bone colonization of disseminated breast cancer cells. *Cancer Cell* **27**, 193–210 (2015).
11. Luo, X. et al. Stromal-initiated changes in the bone promote metastatic niche development. *Cell Rep.* **14**, 82–92 (2016).
12. Yao, Z. et al. Therapy-induced senescence drives bone loss. *Cancer Res.* **80**, 1171–1182 (2020).
13. Nobre, A. R. et al. Bone marrow NG2+/Nestin+ mesenchymal stem cells drive DTC dormancy via TGF-β2. *Nat. Cancer* **2**, 327–339 (2021).
14. Andersen, T. L. et al. A physical mechanism for coupling bone resorption and formation in adult human bone. *Am. J. Pathol.* **174**, 239–247 (2009).
15. Kraemer, B. et al. Impaired bone microenvironment: correlation between bone density and presence of disseminated tumor cells. *Anticancer Res.* **31**, 4423–4428 (2011).
16. Chen, H. M., Chen, F. P., Yang, K. C. & Yuan, S. S. Association of bone metastasis with early-stage breast cancer in women with and without precancer osteoporosis according to osteoporosis therapy status. *JAMA Netw. Open* **2**, e190429 (2019).
17. Blair, H. C. et al. Osteoblast differentiation and bone matrix formation in vivo and in vitro. *Tissue Eng. B Rev.* **23**, 268–280 (2017).
18. Reznikov, N., Bilton, M., Lari, L., Stevens, M. M. & Kröger, R. Fractal-like hierarchical organization of bone begins at the nanoscale. *Science* **360**, eaao2189 (2018).
19. Ping, H. et al. Mineralization generates megapascal contractile stresses in collagen fibrils. *Science* **376**, 188–192 (2022).
20. Choi, S. et al. Intrafibrillar, bone-mimetic collagen mineralization regulates breast cancer cell adhesion and migration. *Biomaterials* **198**, 95–106 (2019).
21. Chaudhuri, O., Cooper-White, J., Janmey, P. A., Mooney, D. J. & Shenoy, V. B. Effects of extracellular matrix viscoelasticity on cellular behaviour. *Nature* **584**, 535–546 (2020).
22. Page, J. M. et al. Matrix rigidity regulates the transition of tumor cells to a bone-destructive phenotype through integrin β3 and TGF-β receptor type II. *Biomaterials* **64**, 33–44 (2015).
23. Turunen, M. J., Prantner, V., Jurvelin, J. S., Kröger, H. & Isaksson, H. Composition and microarchitecture of human trabecular bone change with age and differ between anatomical locations. *Bone* **54**, 118–125 (2013).
24. Donnelly, E., Boskey, A. L., Baker, S. P. & van der Meulen, M. C. H. Effects of tissue age on bone tissue material composition and nanomechanical properties in the rat cortex. *J. Biomed. Mater. Res. A* **92**, 1048–1056 (2010).
25. Burke, M. V., Atkins, A., Akens, M., Willett, T. L. & Whyne, C. M. Osteolytic and mixed cancer metastasis modulates collagen and mineral parameters within rat vertebral bone matrix. *J. Orthop. Res.* **34**, 2126–2136 (2016).
26. Paschalis, E. P., Betts, F., DiCarlo, E., Mendelsohn, R. & Boskey, A. L. FTIR microspectroscopic analysis of normal human cortical and trabecular bone. *Calcif. Tissue Int.* **61**, 480–486 (1997).

27. Mathis, K. M. et al. Bone resorption and bone metastasis risk. *Med. Hypotheses* **118**, 36–41 (2018).
28. Lynch, M. E. et al. In vivo tibial compression decreases osteolysis and tumor formation in a human metastatic breast cancer model. *J. Bone Miner. Res.* **28**, 2357–2367 (2013).
29. Swami, S. et al. Prevention of breast cancer skeletal metastases with parathyroid hormone. *JCI Insight* **2**, e90874 (2017).
30. Farr, J. N. et al. Targeting cellular senescence prevents age-related bone loss in mice. *Nat. Med.* **23**, 1072–1079 (2017).
31. Ooi, L. L. et al. Vitamin D deficiency promotes human breast cancer growth in a murine model of bone metastasis. *Cancer Res.* **70**, 1835–1844 (2010).
32. Wang, H. et al. Bone-in-culture array as a platform to model early-stage bone metastases and discover anti-metastasis therapies. *Nat. Commun.* **8**, 15045 (2017).
33. Fratzl, P., Gupta, H. S., Paschalis, E. P. & Roschger, P. Structure and mechanical quality of the collagen–mineral nano-composite in bone. *J. Mater. Chem.* **14**, 2115–2123 (2004).
34. Gower, L. & Elias, J. Colloid assembly and transformation (CAT): the relationship of PILP to biomineralization. *J. Struct. Biol. X* **6**, 100059 (2022).
35. Chiou, A. E. et al. Fluorescent silica nanoparticles to label metastatic tumor cells in mineralized bone microenvironments. *Small* **17**, e2001432 (2021).
36. Carlson, P. et al. Targeting the perivascular niche sensitizes disseminated tumour cells to chemotherapy. *Nat. Cell Biol.* **21**, 238–250 (2019).
37. Olszta, M. J. et al. Bone structure and formation: a new perspective. *Mater. Sci. Eng. R* **58**, 77–116 (2007).
38. Reznikov, N., Chase, H., Brumfeld, V., Shahar, R. & Weiner, S. The 3D structure of the collagen fibril network in human trabecular bone: relation to trabecular organization. *Bone* **71**, 189–195 (2015).
39. Londoño-Restrepo, S. M., Jeronimo-Cruz, R., Millán-Malo, B. M., Rivera-Muñoz, E. M. & Rodriguez-García, M. E. Effect of the nano crystal size on the X-ray diffraction patterns of biogenic hydroxyapatite from human, bovine, and porcine bones. *Sci. Rep.* **9**, 5915 (2019).
40. Nam, S., Lee, J., Brownfield, D. G. & Chaudhuri, O. Viscoplasticity enables mechanical remodeling of matrix by cells. *Biophys. J.* **111**, 2296–2308 (2016).
41. Hall, M. S. et al. Fibrous nonlinear elasticity enables positive mechanical feedback between cells and ECMs. *Proc. Natl Acad. Sci. USA* **113**, 14043–14048 (2016).
42. Masuda, T. et al. ANGPTL2 increases bone metastasis of breast cancer cells through enhancing CXCR4 signaling. *Sci. Rep.* **5**, 9789 (2015).
43. Bergamaschi, A. et al. CAMK1D amplification implicated in epithelial-mesenchymal transition in basal-like breast cancer. *Mol. Oncol.* **2**, 327–339 (2008).
44. Dong, X., Yang, Y., Yuan, Q., Hou, J. & Wu, G. High expression of CEMIP correlates poor prognosis and the tumor microenvironment in breast cancer as a promisingly prognostic biomarker. *Front. Genet.* **12**, 768140 (2021).
45. Che, M. I. et al. β1, 4-N-acetylgalactosaminyltransferase III modulates cancer stemness through EGFR signaling pathway in colon cancer cells. *Oncotarget* **5**, 3673–3684 (2014).
46. Yu, J. M. et al. TRIB3 supports breast cancer stemness by suppressing FOXO1 degradation and enhancing SOX2 transcription. *Nat. Commun.* **10**, 5720 (2019).
47. Choate, J. J. & Mosher, D. F. Fibronectin concentration in plasma of patients with breast cancer, colon cancer, and acute leukemia. *Cancer* **51**, 1142–1147 (1983).
48. Pathi, S. P., Lin, D. D. W., Dorvee, J. R., Estroff, L. A. & Fischbach, C. Hydroxyapatite nanoparticle-containing scaffolds for the study of breast cancer bone metastasis. *Biomaterials* **32**, 5112–5122 (2011).
49. Bruning, P. F. et al. Bone mineral density after adjuvant chemotherapy for premenopausal breast cancer. *Br. J. Cancer* **61**, 308–310 (1990).
50. Balestrini, J. L., Chaudhry, S., Sarrazy, V., Koehler, A. & Hinz, B. The mechanical memory of lung myofibroblasts. *Integr. Biol.* **4**, 410–421 (2012).
51. Li, C. X. et al. MicroRNA-21 preserves the fibrotic mechanical memory of mesenchymal stem cells. *Nat. Mater.* **16**, 379–389 (2016).
52. He, F. et al. Hydroxyapatite mineral enhances malignant potential in a tissue-engineered model of ductal carcinoma in situ (DCIS). *Biomaterials* **224**, 119489 (2019).
53. Chiou, A. E. et al. Breast cancer-secreted factors perturb murine bone growth in regions prone to metastasis. *Sci. Adv.* **7**, eabf2283 (2021).
54. Zhang, W. et al. The bone microenvironment invigorates metastatic seeds for further dissemination. *Cell* **184**, 2471–2486. e20 (2021).
55. Thiagarajan, P. S. et al. Development of a fluorescent reporter system to delineate cancer stem cells in triple-negative breast cancer. *Stem Cells* **33**, 2114–2125 (2015).
56. Ginestier, C. et al. ALDH1 is a marker of normal and malignant human mammary stem cells and a predictor of poor clinical outcome. *Cell Stem Cell* **1**, 555–567 (2007).
57. Raha, D. et al. The cancer stem cell marker aldehyde dehydrogenase is required to maintain a drug-tolerant tumor cell subpopulation. *Cancer Res.* **74**, 3579–3590 (2014).
58. Pan, G. et al. A negative feedback loop of transcription factors that controls stem cell pluripotency and self-renewal. *FASEB J.* **20**, 1730–1732 (2006).
59. Krishnakumar, R. et al. FOXD3 regulates pluripotent stem cell potential by simultaneously initiating and repressing enhancer activity. *Cell Stem Cell* **18**, 104–117 (2016).
60. Chu, T. L. et al. FoxD3 deficiency promotes breast cancer progression by induction of epithelial–mesenchymal transition. *Biochem. Biophys. Res. Commun.* **446**, 580–584 (2014).
61. Li, W. et al. Unraveling the roles of CD44/CD24 and ALDH1 as cancer stem cell markers in tumorigenesis and metastasis. *Sci. Rep.* **7**, 13856 (2017).
62. Paszek, M. J. et al. Tensional homeostasis and the malignant phenotype. *Cancer Cell* **8**, 241–254 (2005).
63. Seo, B. R. et al. Collagen microarchitecture mechanically controls myofibroblast differentiation. *Proc. Natl Acad. Sci. USA* **117**, 11387–11398 (2020).
64. Barney, L. E. et al. Tumor cell-organized fibronectin maintenance of a dormant breast cancer population. *Sci. Adv.* **6**, eaaz4157 (2020).
65. Reznikov, N. et al. Biological stenciling of mineralization in the skeleton: local enzymatic removal of inhibitors in the extracellular matrix. *Bone* **138**, 115447 (2020).
66. Boys, A. J. et al. Top-down fabrication of spatially controlled mineral-gradient scaffolds for interfacial tissue engineering. *ACS Biomater. Sci. Eng.* https://doi.org/10.1021/acsbiomaterials.9b00176 (2019).
67. Zhou, H., Boys, A. J., Harrod, J. B., Bonassar, L. J. & Estroff, L. A. Mineral distribution spatially patterns bone marrow stromal cell behavior on monolithic bone scaffolds. *Acta Biomater.* **112**, 274–285 (2020).
68. Fornetti, J., Welm, A. L. & Stewart, S. A. Understanding the bone in cancer metastasis. *J. Bone Miner. Res.* **33**, 2099–2113 (2018).
69. Crapo, P. M., Gilbert, T. W. & Badylak, S. F. An overview of tissue and whole organ decellularization processes. *Biomaterials* **32**, 3233–3243 (2011).

70. Gao, Y. et al. Metastasis organotropism: redefining the congenial soil. *Dev. Cell* **49**, 375–391 (2019).
71. Cox, T. R. The matrix in cancer. *Nat. Rev. Cancer* **21**, 217–238 (2021).
72. Reuten, R. et al. Basement membrane stiffness determines metastases formation. *Nat. Mater.* **20**, 892–903 (2021).
73. Nam, S., Hu, K. H., Butte, M. J. & Chaudhuri, O. Strain-enhanced stress relaxation impacts nonlinear elasticity in collagen gels. *Proc. Natl Acad. Sci. USA* **113**, 5492–5497 (2016).
74. Aguirre-Ghiso, J. A., Liu, D., Mignatti, A., Kovalski, K. & Ossowski, L. Urokinase receptor and fibronectin regulate the ERK(MAPK) to p38(MAPK) activity ratios that determine carcinoma cell proliferation or dormancy in vivo. *Mol. Biol. Cell* **12**, 863–879 (2001).
75. Margadant, C. & Sonnenberg, A. Integrin-TGF-B crosstalk in fibrosis, cancer and wound healing. *EMBO Rep.* **11**, 97–105 (2010).
76. Ruppender, N. et al. Cellular adhesion promotes prostate cancer cells escape from dormancy. *PLoS ONE* **10**, e0130565 (2015).
77. Bragado, P. et al. TGF-β2 dictates disseminated tumour cell fate in target organs through TGF-β-RIII and p38α/β signalling. *Nat. Cell Biol.* **15**, 1351–1361 (2013).
78. Sosa, M. S. et al. NR2F1 controls tumour cell dormancy via SOX9- and RARβ-driven quiescence programmes. *Nat. Commun.* **6**, 6170 (2015).
79. Marturano-Kruik, A. et al. Human bone perivascular niche-on-a-chip for studying metastatic colonization. *Proc. Natl Acad. Sci. USA* **115**, 1256–1261 (2018).
80. Thrivikraman, G. et al. Rapid fabrication of vascularized and innervated cell-laden bone models with biomimetic intrafibrillar collagen mineralization. *Nat. Commun.* **10**, 3520 (2019).
81. Singh, D. K., Patel, V. G., Oh, W. K. & Aguirre-Ghiso, J. A. Prostate cancer dormancy and reactivation in bone marrow. *J. Clin. Med.* **10**, 2648 (2021).
82. Boskey, A. L. & Coleman, R. Critical reviews in oral biology and medicine: aging and bone. *J. Dent. Res.* **89**, 1333–1348 (2010).
83. Azarin, S. M. et al. In vivo capture and label-free detection of early metastatic cells. *Nat. Commun.* **6**, 8094 (2015).
84. Sadtler, K. et al. Divergent immune responses to synthetic and biological scaffolds. *Biomaterials* **192**, 405–415 (2019).
85. Coleman, R. et al. Adjuvant bisphosphonate treatment in early breast cancer: meta-analyses of individual patient data from randomised trials. *Lancet* **386**, 1353–1361 (2015).
86. Coleman, R. E. et al. Breast-cancer adjuvant therapy with zoledronic acid. *N. Engl. J. Med.* **365**, 1396–1405 (2011).
87. Pelham, R. J. & Wang, Y. L. Cell locomotion and focal adhesions are regulated by substrate flexibility. *Proc. Natl Acad. Sci. USA* **94**, 13661 (1997).
88. Przybyla, L., Lakins, J. N., Sunyer, R., Trepat, X. & Weaver, V. M. Monitoring developmental force distributions in reconstituted embryonic epithelia. *Methods* **94**, 101–113 (2016).
89. Han, S. J., Oak, Y., Groisman, A. & Danuser, G. Traction microscopy to identify force modulation in subresolution adhesions. *Nat. Methods* **12**, 653–656 (2015).
90. Dobin, A. & Gingeras, T. R. Mapping RNA-seq reads with STAR. *Curr. Protoc. Bioinformatics* **51**, 11.14.1–11.14.19 (2015).
91. Liao, Y., Smyth, G. K. & Shi, W. featureCounts: an efficient general purpose program for assigning sequence reads to genomic features. *Bioinformatics* **30**, 923–930 (2014).
92. Love, M. I., Huber, W. & Anders, S. Moderated estimation of fold change and dispersion for RNA-seq data with DESeq2. *Genome Biol.* **15**, 550 (2014).
93. Grüneboom, A. et al. A network of *trans*-cortical capillaries as mainstay for blood circulation in long bones. *Nat .Metab.* **1**, 236–250 (2019).
94. Bankhead, P. et al. QuPath: open source software for digital pathology image analysis. *Sci. Rep.* **7**, 16878 (2017).

Acknowledgements

We thank all members of the Fischbach lab for valuable discussions of this research; the Wiesner group (Cornell University) for providing fluorescent silica nanoparticles; J. Kuo (Cornell University) for help with illustrations; L. O'Keeffe for help with preparation of bone scaffolds; the Cornell Animal Health Diagnostic Core for paraffin embedding and sectioning; J. Massague (Memorial Sloan Kettering Cancer Center) for providing bone tropic BoM1-2287 and BoM-1833; and the Cornell Center for Animal Resources and Education (CARE) staff for animal care. Financial support was provided by the Human Frontier Science Program (RGP0016/2017); the National Cancer Institute through the Center on the Physics of Cancer Metabolism (1U54CA210184); NIH F31 (F31CA228448) to A.E.C.; fellowship support by the Stem Cell Program of Cornell University to N.D.S.; and NSF GRFP (DGE-1650441) to M.A.W. and A.A.S. This work used the Cornell Center for Materials Research (CCMR), which is supported through the NSF MRSEC program (DMR-1719875); the Cornell NanoScale Science & Technology Facility (CNF), a member of the NSF-supported National Nanotechnology Coordinated Infrastructure (NNCI-2025233); and the Cornell University Biotechnology Resource Center (BRC) facilities, including a Zeiss LSM 710 confocal microscope (NIH 1S10RR025502), Zeiss LSM880 confocal/multiphoton microscope (NYSTEM (C029155) and NIH (S10OD018516)), light-sheet microscope (NIH S10OD023466), ZEISS/Xradia Versa 520 X-ray microscope (NIH S10OD012287), IVIS Spectrum (NIH S10OD025049) and Genomics Facility (RRID:SCR_021727).

Author contributions

S.C., M.A.W., L.A.E. and C.F. designed the project. S.C. and M.A.W. conducted most of the experiments. A.A.S. performed and analysed FACS and RNA-seq data. N.D.S performed and analysed the hMSC experiments. A.E.C. performed the animal study for light-sheet microscopy. J.E.D. performed FACS. A.V. and O.E. analysed RNA-seq data with the SSGSEA method. S.C.L. analysed IHC images. Z.C, A.A.S. and M.P. conducted and analysed TFM. S.C., M.A.W., L.A.E. and C.F. analysed the data and wrote the paper. All authors discussed the results and commented on the paper.

Competing interests

O.E. was supported by Janssen, J&J, Astra-Zeneca, Volastra and Eli Lilly research grants. He is scientific advisor and equity holder in Freenome, Owkin, Volastra Therapeutics and One Three Biotech, and a paid scientific advisor to Champions Oncology and Pionyr Therapeutics. The other authors declare no competing interests.

Additional information

Extended data is available for this paper at https://doi.org/10.1038/s41551-023-01077-3.

Supplementary information The online version contains supplementary material available at https://doi.org/10.1038/s41551-023-01077-3.

Correspondence and requests for materials should be addressed to Lara A. Estroff or Claudia Fischbach.

Peer review information *Nature Biomedical Engineering* thanks Julie A. Rhoades, Hai Wang and the other, anonymous, reviewer(s) for their contribution to the peer review of this work.

https://doi.org/10.1038/s41551-023-01077-3

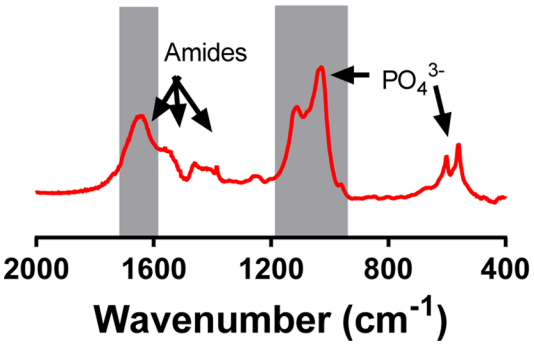

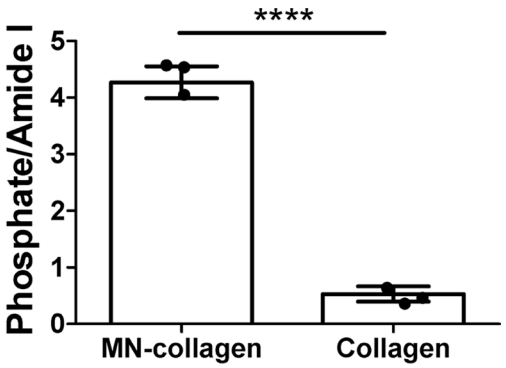

Extended Data Fig. 1 | Mineral-to-matrix ratio of collagen and mineralized collagen. Mineral to matrix ratio of mineralized collagen as calculated by dividing the phosphate peak area (907–1183 cm^{-1}) of FT-IR spectra by the amide I peak area (1580–1727 cm^{-1}) ($n = 3$; $^{****}p < 0.0001$). Data are mean ± SD. Data were calculated using two-tailed unpaired *t*-test.

https://doi.org/10.1038/s41551-023-01077-3

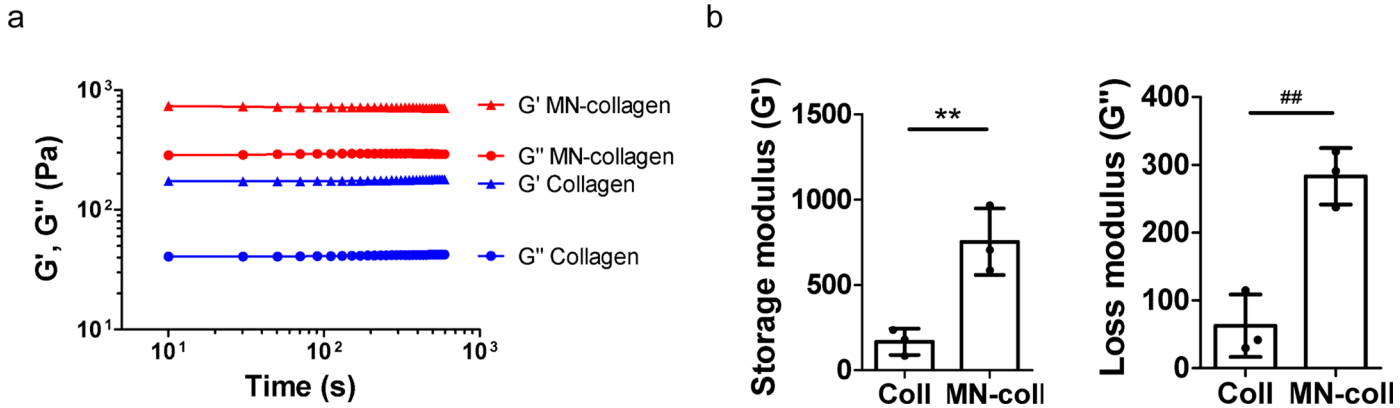

Extended Data Fig. 2 | Storage and loss moduli of collagen and mineralized collagen. a, b, Representative time sweeps (**a**) and quantification of storage (G′) and loss (G″) moduli ($n = 3$; $^{**}p = 0.0083$; $^{\#\#}p = 0.0035$) (**b**). Data are mean ± SD. Data in **b** were calculated using two-tailed unpaired *t*-test.

https://doi.org/10.1038/s41551-023-01077-3

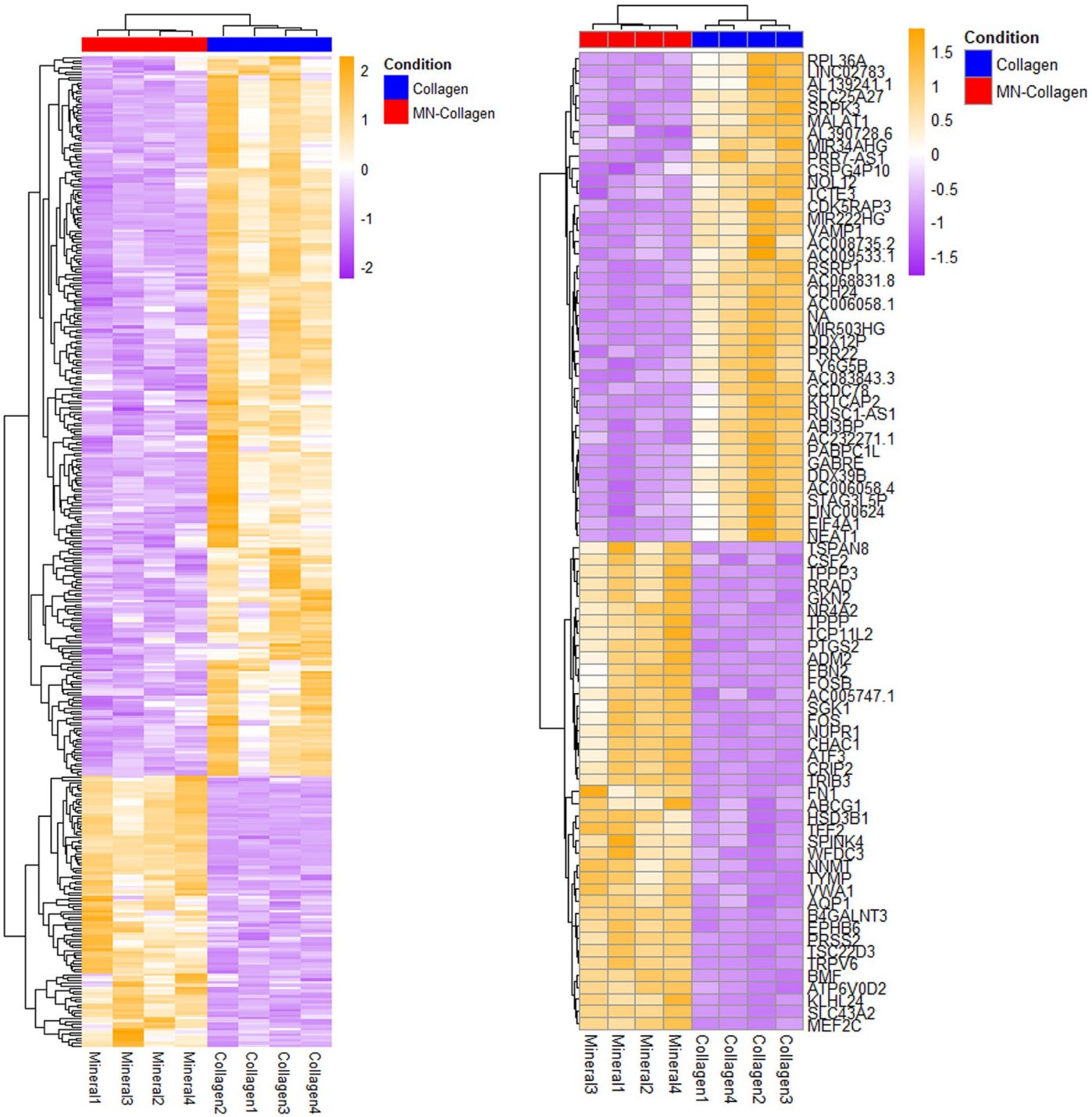

Extended Data Fig. 3 | Heatmap of differentially expressed genes (DEGs). DEGs were defined as the genes with FDR-adjusted p-values < 0.05 and $\log_2$FC > 1. Relative expression levels of all DEGs (left) or top 50 genes (right) is split into collagen and mineralized collagen conditions.

https://doi.org/10.1038/s41551-023-01077-3

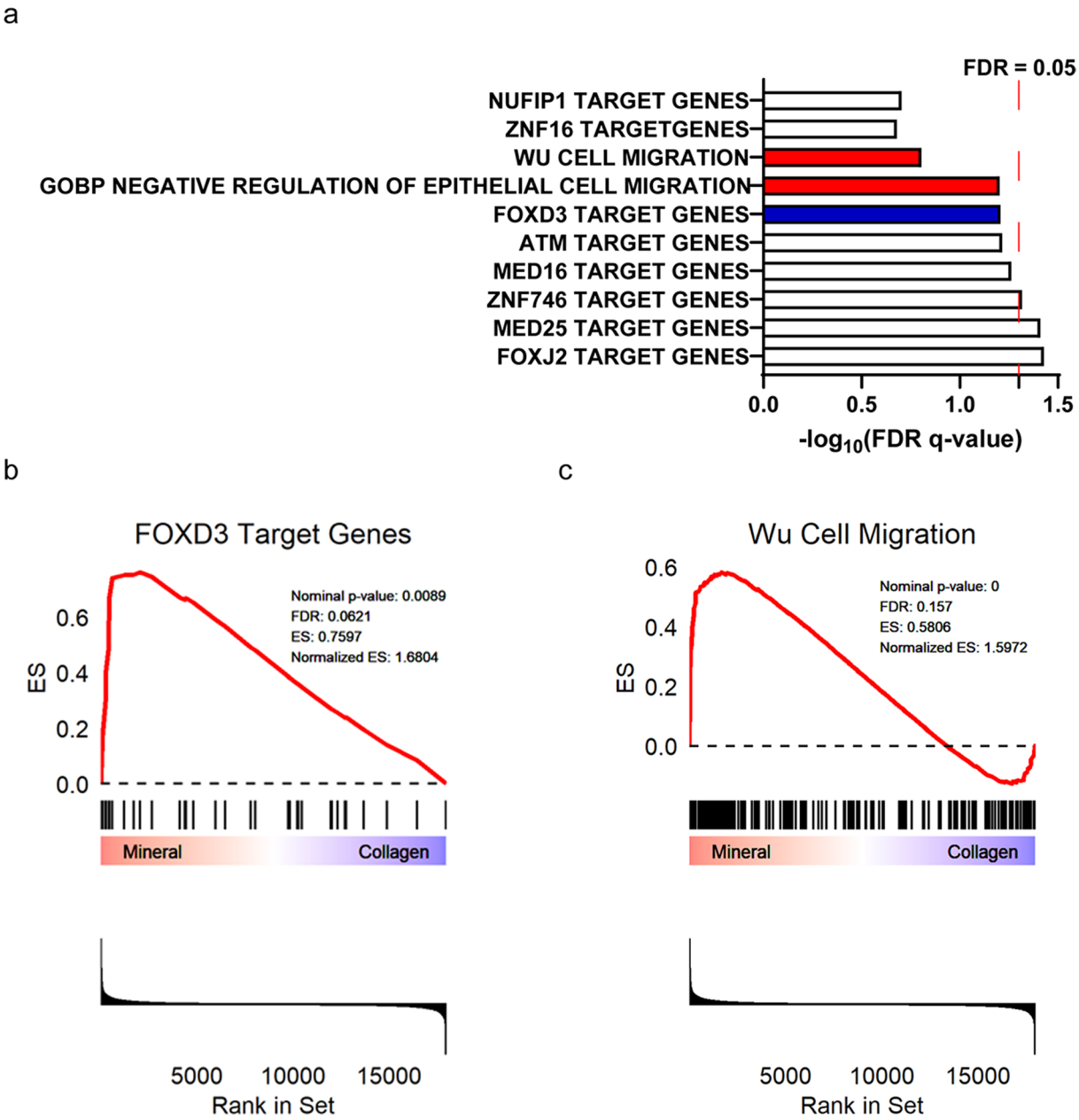

Extended Data Fig. 4 | Top-10 enrichment plot from gene-set enrichment analysis (GSEA). a, GSEA indicates that biological processes associated with transcription and cell migration were overrepresented by collagen mineralization. Red labeled gene sets are associated with actin remodeling and migration curated from the Molecular Signatures Data Base (MSigDB), while blue labeled gene sets have been directly linked to stemness. The top 3 significant transcription factors (*FOXJ2, MED25, ZNF746*) do not have clearly defined functions beyond complexing with RNA polymerase II but *FOXD3* was also enriched albeit to a less significant extent (FDR q-value = 0.062). Dashed red line designates FDR q-value cutoff of 0.05. **b**, Enrichment plot for FOXD3 target genes as determined by GSEA. Normalized Enrichment Score (NES) = 1.68, nominal p-value = 0.009, FDR q-value = 0.062. **c**, Enrichment plot for the Wu Cell Migration gene signature from the MSigDB as determined by GSEA. Normalized Enrichment Score (NES) = 1.60, nominal p-value < 0.001, FDR q-value = 0.157. While cell migration was not a focus of our study, this gene set includes several genes directly related to cytoskeletal remodeling (for example *NEDD9*, *KRT19, S100A4*, and *FN1*).

https://doi.org/10.1038/s41551-023-01077-3

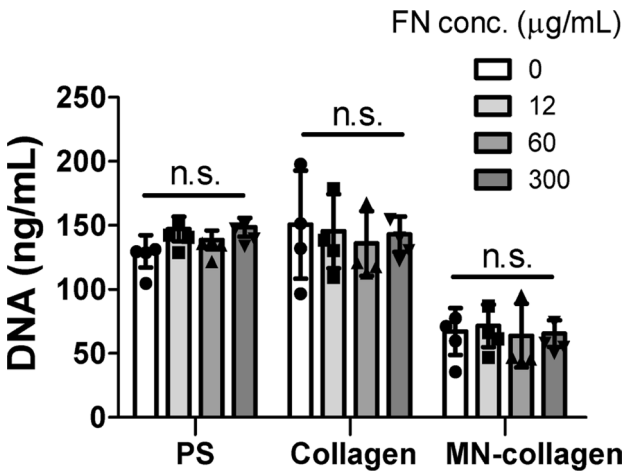

Extended Data Fig. 5 | Pre-adsorbed fibronectin does not affect the growth of MDA-MB231. MDA-MB231 cell growth on the different substrates for 7 d. Substrates were incubated with various concentrations of fibronectin (FN) before cell seeding ($n = 4$). Data are mean ± SD. Data were calculated using two-way ANOVA with Tukey's multiple comparisons.

https://doi.org/10.1038/s41551-023-01077-3

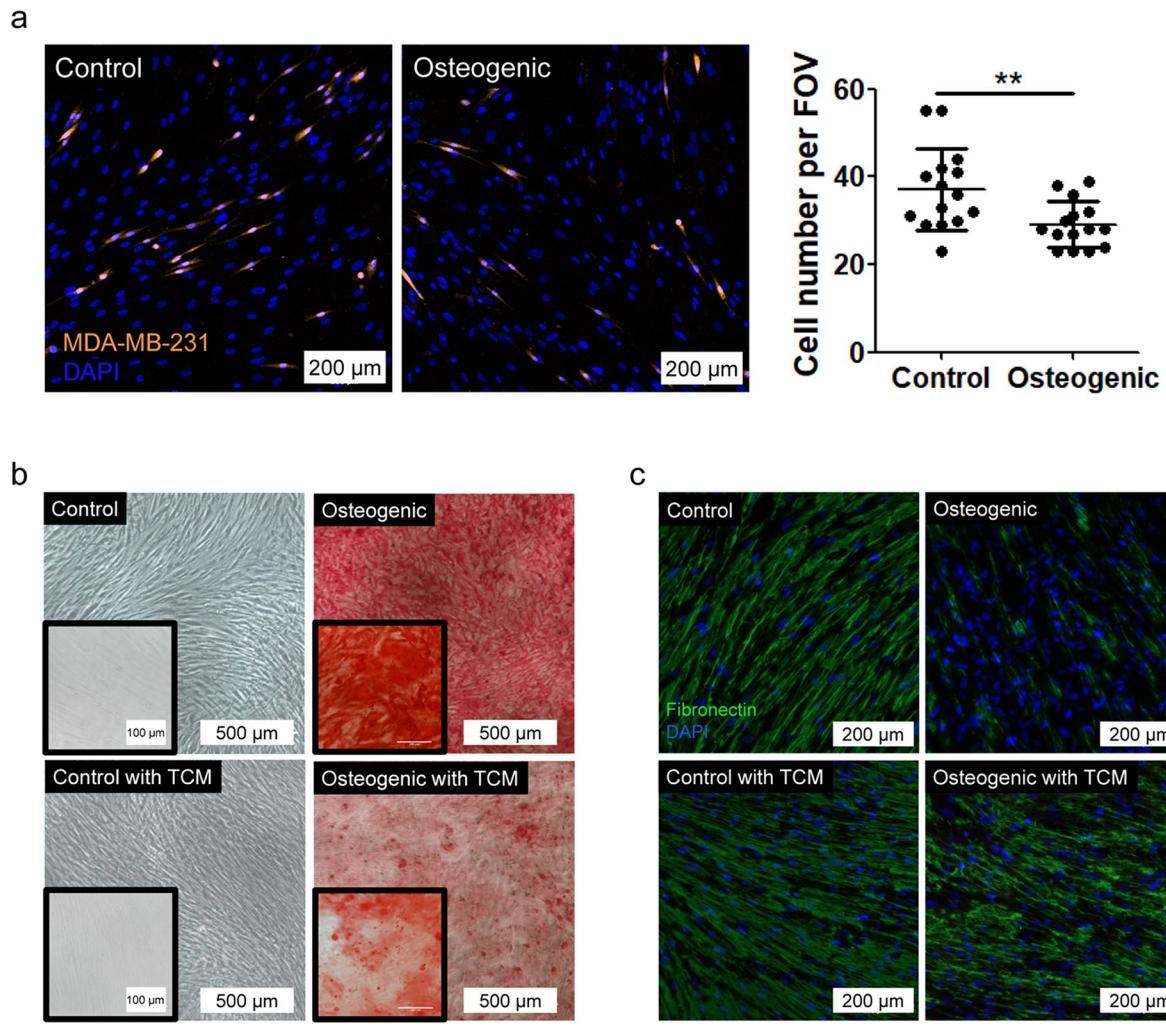

Extended Data Fig. 6 | Matrix mineralization correlates with decreased tumour-cell growth in the presence of bone-resident cells. a, Representative confocal micrographs and corresponding quantification of co-cultured osteogenically differentiated hMSCs and labeled MDA-MB231 cells ($n = 3$; $^{**}p = 0.0061$). Scale bar = 200 µm. **b**, Representative bright field micrographs of Alizarin Red S stained hMSCs cultured with control or osteogenic media and in the presence or absence of tumor-conditioned media (TCM). Scale bar, 500 µm and 100 µm (inset). **c**, Representative confocal micrographs of hMSCs stained for fibronectin. Scale bar = 200 µm. Data are mean ± SD. Data in **a** were calculated using two-tailed Mann Whitney U test.

https://doi.org/10.1038/s41551-023-01077-3

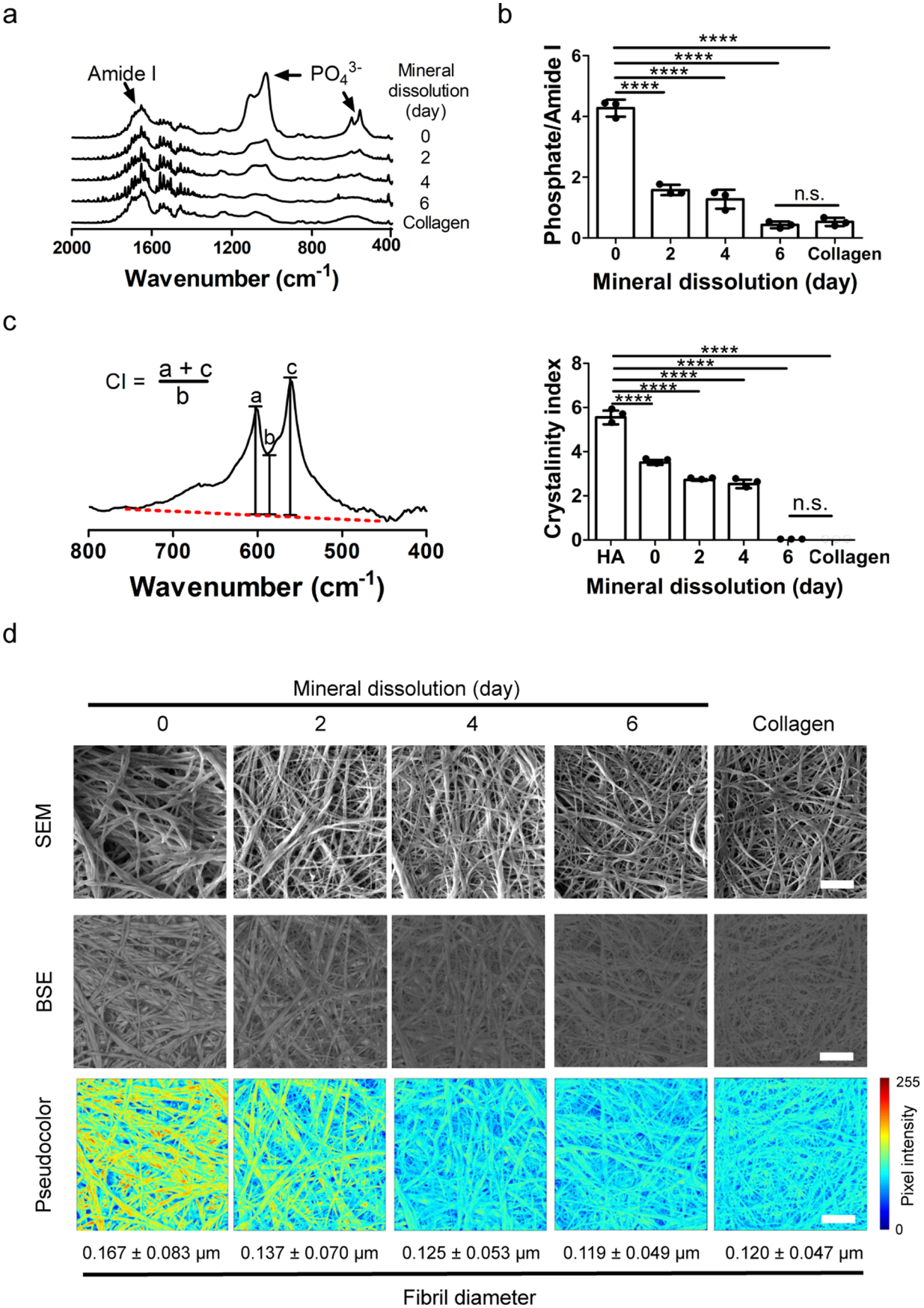

Extended Data Fig. 7 | See next page for caption.

https://doi.org/10.1038/s41551-023-01077-3

Extended Data Fig. 7 | Characterization of mineralized collagen at different time points of dissolution. a, FT-IR spectra of mineralized collagen following hydroxyapatite dissolution for up to 6 days. Non-mineralized collagen served as control. **b,c**, FT-IR analysis of mineral to matrix ratio ($n = 3$; $^{****}p < 0.0001$) (**b**) and crystallinity index (CI) of matrices after different periods of mineral dissolution ($n = 3$; $^{****}p < 0.0001$) (**c**). CI was calculated by drawing a baseline between 450 cm^{-1} and 750 cm^{-1} (red dashed line) and measuring the heights of phosphate peaks at 567 cm^{-1} and 603 cm^{-1} and the height of the lowest point between them relative to the baseline. **d**, Representative SEM and BSE images visualizing differences in mineral content and collagen fibril diameter after different periods of mineral dissolution. Pseudocolor was generated from BSE images by converting grey-scale pixel intensity to a linear 256-bit color scale. Fibril diameter was measured from SEM images. Scale bar = 2 µm. Data are mean ± SD. Data in **b** and **c** were calculated using one-way ANOVA with Dunnett's multiple comparisons.

https://doi.org/10.1038/s41551-023-01077-3

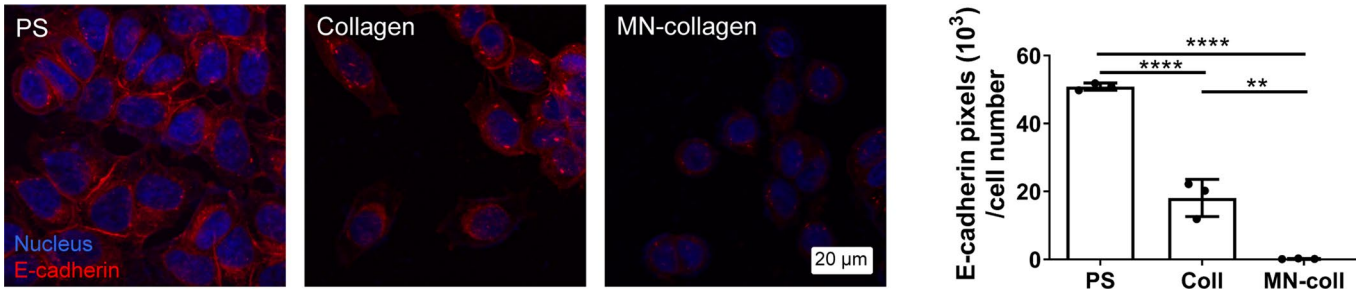

Extended Data Fig. 8 | E-cadherin expression of MCF7 is reduced by mineralized collagen. Representative confocal micrographs and corresponding quantification of E-cadherin after 7 d of culture of MCF7 cells on the different substrates ($n = 3$; $^{**}p = 0.0012$; $^{****}p < 0.0001$). Scale bar = 20 µm. Data are mean ± SD. Data were calculated using one-way ANOVA with Tukey's multiple comparisons.

https://doi.org/10.1038/s41551-023-01077-3

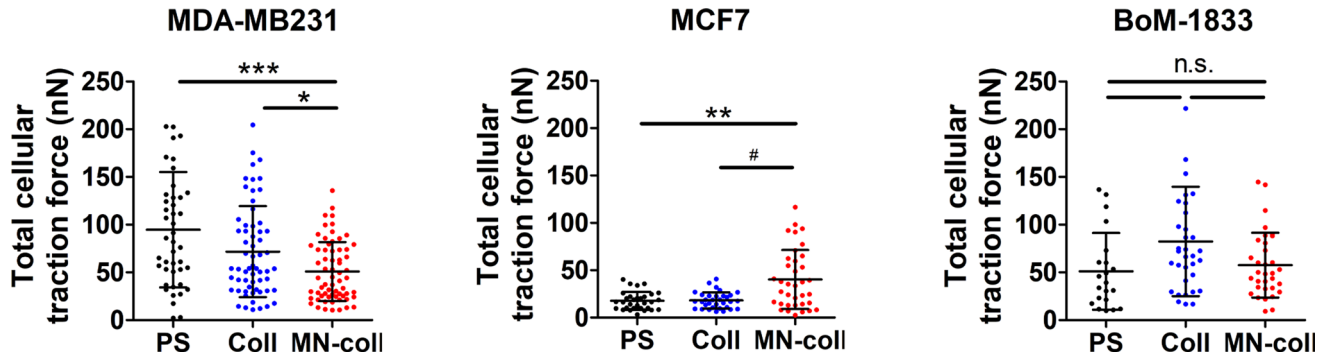

Extended Data Fig. 9 | Total traction forces of different breast-cancer cell lines. Cells were precultured on tissue culture polystyrene (PS), collagen, and mineralized collagen. Cells were precultured on the different substrates for 7 days prior to reseeding on PA gels for traction force microscopy measurements (MDA-MB231 (PS: 44 cells examined from 3 gels; Col and MN-col: at least 61 cells examined from 6 gels); MCF7 (at least 31cells examined from 5 gels); BoM-1833 (PS: 21 cells examined from 2 gels; Col and MN-col: at least 33 cells examined from 3 gels)). $^{*}p = 0.0459$; $^{**}p = 0.0076$; $^{***}p = 0.0001$; $^{\#}p = 0.0193$. Data are mean ± SD. Data were calculated using Kruskal Wallis test with Dunn's multiple comparisons.

https://doi.org/10.1038/s41551-023-01077-3

a

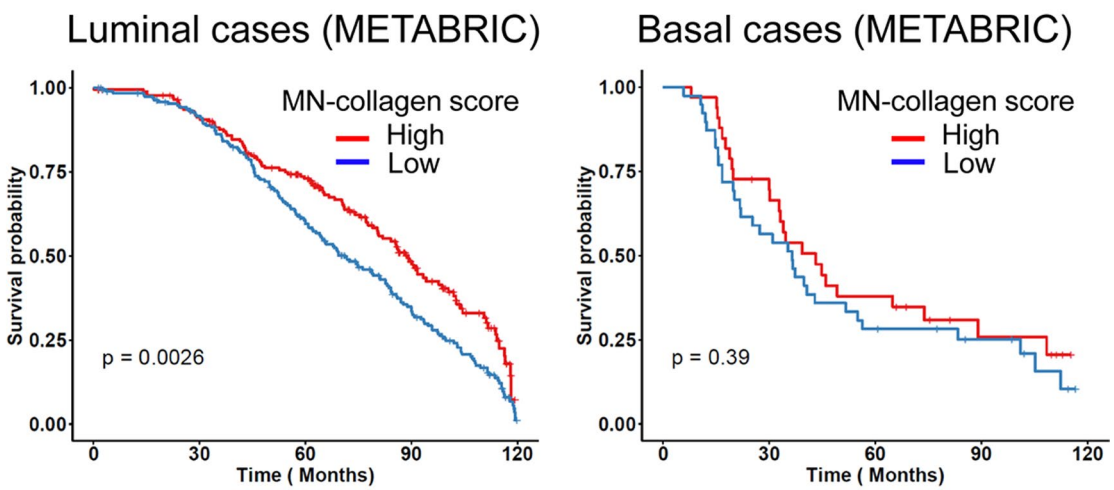

b

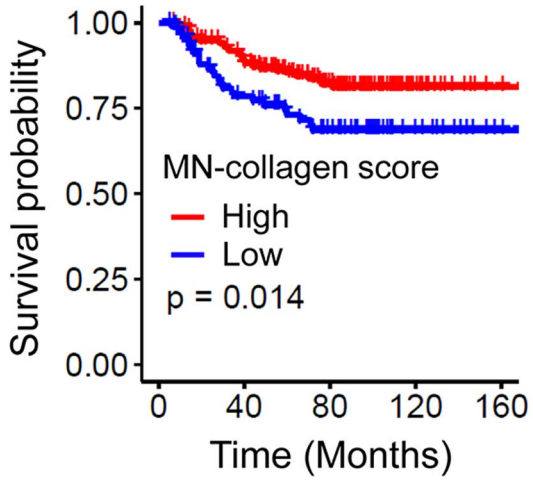

Extended Data Fig. 10 | Survival analysis of patients with breast cancer. **a**, Overall survival of patients with breast cancer by stratification based on mineral-induced gene expression using different breast cancer subtypes in METABRIC database. **b**, Overall bone metastasis-free survival of patients with breast cancer scoring high or low for expression of the mineral-induced gene signature (Supplementary Table 2).

nature portfolio

Corresponding author(s): Claudia Fischbach-Teschl, Lara A. Estroff

Last updated by author(s): April 13, 2023

Reporting Summary

Nature Portfolio wishes to improve the reproducibility of the work that we publish. This form provides structure for consistency and transparency in reporting. For further information on Nature Portfolio policies, see our Editorial Policies and the Editorial Policy Checklist.

Statistics

For all statistical analyses, confirm that the following items are present in the figure legend, table legend, main text, or Methods section.

n/a	Confirmed
☐	☒ The exact sample size (*n*) for each experimental group/condition, given as a discrete number and unit of measurement
☐	☒ A statement on whether measurements were taken from distinct samples or whether the same sample was measured repeatedly
☐	☒ The statistical test(s) used AND whether they are one- or two-sided *Only common tests should be described solely by name; describe more complex techniques in the Methods section.*
☒	☐ A description of all covariates tested
☒	☐ A description of any assumptions or corrections, such as tests of normality and adjustment for multiple comparisons
☐	☒ A full description of the statistical parameters including central tendency (e.g. means) or other basic estimates (e.g. regression coefficient) AND variation (e.g. standard deviation) or associated estimates of uncertainty (e.g. confidence intervals)
☐	☒ For null hypothesis testing, the test statistic (e.g. *F*, *t*, *r*) with confidence intervals, effect sizes, degrees of freedom and *P* value noted *Give P values as exact values whenever suitable.*
☒	☐ For Bayesian analysis, information on the choice of priors and Markov chain Monte Carlo settings
☒	☐ For hierarchical and complex designs, identification of the appropriate level for tests and full reporting of outcomes
☒	☐ Estimates of effect sizes (e.g. Cohen's *d*, Pearson's *r*), indicating how they were calculated

Our web collection on statistics for biologists contains articles on many of the points above.

Software and code

Policy information about availability of computer code

Data collection	Characterization of mineralized collagen and scaffolds: SEM (Mira3 LM); FT-IR (Hyperion2000/Tensor27); XRD (D8 advance ECO powder diffractometer); X-ray microscope (Xradia Zeiss Versa XRM-520); SHG microscopy (Zeiss LSM880). Analysis of tumour-cell phenotype: Confocal microscopy (Zeiss LSM810; Zeiss LSM880; Zeiss LSM710); Western Blot and sphere formation (ChemiDoc TM Touch Imaging System); Flow cytometry (BD Accuri C6 Plus); RNA sequencing (NextSeqS00). Animal studies: Light-sheet microscopy (LaVision BioTec); Ultrasound guidance (Vevo VisualSonics 2100); Bioluminescence imaging (IVIS Spectrum). Tissue imaging: ScanScope slide scanner (Aperio CS2).
Data analysis	Statistic analysis and data plotting: PRISM v9.5.0. Mineral-to-matrix-ratio analysis from FT-IR: OPUS 6.5. Western Blot and sphere formation: Imaging Lab 6.0. Flow cytometry: FCS Express: 6.06.0042. RNA sequencing: STAR v2.6.0a. Tissue analysis: QuPath v0.2.0. Image analysis and processing: MATLAB, ImageJ, and Arivis Vision 4D. Bioluminescence analysis: LivingImage.

For manuscripts utilizing custom algorithms or software that are central to the research but not yet described in published literature, software must be made available to editors and reviewers. We strongly encourage code deposition in a community repository (e.g. GitHub). See the Nature Portfolio guidelines for submitting code & software for further information.

Data

Policy information about availability of data

All manuscripts must include a data availability statement. This statement should provide the following information, where applicable:

- Accession codes, unique identifiers, or web links for publicly available datasets
- A description of any restrictions on data availability
- For clinical datasets or third party data, please ensure that the statement adheres to our policy

The main data supporting the results in this study are available within the paper and its Supplementary Information. All RNA sequencing data generated in this study are available in the NIH Gene Expression Omnibus via the accession number GSE229094. Survival analysis was conducted using publicly available datasets (Study ID: GEO2603, GSE2034). Source data for the figures are provided with this paper.

Human research participants

Policy information about studies involving human research participants and Sex and Gender in Research.

Reporting on sex and gender	The study did not involve human research participants.
Population characteristics	—
Recruitment	—
Ethics oversight	—

Note that full information on the approval of the study protocol must also be provided in the manuscript.

Field-specific reporting

Please select the one below that is the best fit for your research. If you are not sure, read the appropriate sections before making your selection.

☒ Life sciences ☐ Behavioural & social sciences ☐ Ecological, evolutionary & environmental sciences

For a reference copy of the document with all sections, see nature.com/documents/nr-reporting-summary-flat.pdf

Life sciences study design

All studies must disclose on these points even when the disclosure is negative.

Sample size	Sample sizes were based on our previous experience and on pilot studies. For the in vivo studies, sample size was validated using a power analysis. The number of samples and of independent replicates is indicated in the paper (in the statistical-analysis section or specified in the respective data-analysis sections for traction force microscopy and for the animal studies).
Data exclusions	A single outlier was identified in the BLI data via a Grubb's test with a significance level of alpha = 0.0001, and excluded accordingly, to avoid skewing the dataset. For traction-force data, a single data point was identified as an outlier using the ROUT method with a Q value of 1%, and was excluded to avoid skewing.
Replication	All experiments were performed with at least 3 independent replicates. All attempts at replication were successful.
Randomization	For the in vivo experiments, each mouse received scaffolds of each scaffold type to control for animal-specific variation. Additionally, the implant location of each matrix condition was alternated per mouse such that each implant location was equally represented across mice and across experimental conditions. Mice were randomly assigned to groups.
Blinding	Immunohistochemistry and bioluminescence-image analysis were done in a blinded manner. The images were anonymized for quantification and subsequently grouped for statistical analysis.

Reporting for specific materials, systems and methods

We require information from authors about some types of materials, experimental systems and methods used in many studies. Here, indicate whether each material, system or method listed is relevant to your study. If you are not sure if a list item applies to your research, read the appropriate section before selecting a response.

Materials & experimental systems

n/a	Involved in the study
☐	☒ Antibodies
☐	☒ Eukaryotic cell lines
☒	☐ Palaeontology and archaeology
☐	☒ Animals and other organisms
☒	☐ Clinical data
☒	☐ Dual use research of concern

Methods

n/a	Involved in the study
☒	☐ ChIP-seq
☐	☒ Flow cytometry
☒	☐ MRI-based neuroimaging

Antibodies

Antibodies used

For Western blot: rabbit-anti-human Sox2 (S9072, Sigma Aldrich); rabbit-anti-human Oct4 (AB3209, Millipore); rabbit-anti-human HSP90 (sc-7947, Santa Cruz).
For mechanosignalling blocking: mouse-anti-human B1 integrin clone 6S6 (MAB2253Z, Millipore).
For cell and tissue staining: rabbit-anti-human ki67 (9027S, Cell Signaling Technologies); rabbit anti-human vimentin (MA5-16409, Thermo Fisher Scientific); AP-conjugated horse anti-rabbit IgG (MP-5401-15, Vector Labs); HRP-conjugated horse anti-rabbit IgG (MP-7401, Vector Labs); mouse anti-human E-cadherin (61081, BS Biosciences); APC-conjugated anti-human CD44 clone G44-26 (555745, BD Biosciences); PE-Cy7-conjugated anti-CD24 clone ML5 (561646, BD Biosciences); APC-conjugated mouse anti-IgG2b clone 27-35 (555745, BD Biosciences); PE-Cy7-conjugated mouse anti-IgG2a clone G155-178 (557907, BD Biosciences); mouse anti-human fibronectin (F7387, Sigma Aldrich); goat anti-mouse Alexa Fluor 568 (A11004, Thermo Fisher Scientific); goat anti-mouse Alexa Fluor 488 (A11001, Thermo Fisher Scientific).

Validation

All antibodies are commercially available and validated by their respective vendors. Individual protocols were developed for each antibody using appropriate isotype controls, and antibody performance and reproducibility is routinely verified in our lab by multiple users using similar model systems. No additional validation was done.

Eukaryotic cell lines

Policy information about cell lines and Sex and Gender in Research

Cell line source(s)

The MDA-MB231 and MCF-7 cell lines were procured from ATCC.
MDA-MB231 cells expressing the Nanog-GFP reporter were generated and provided by Ofer Reizes, and the bone metastatic BoM1-2287 and BOM1-1833 cell lines were provided by Joan Massague.

Authentication

The cell lines sourced from ATCC were authenticated by STR profiling.
RoosterBio hMSCs were authenticated by the manufacturer to meet ISCT minimum criteria for hMSC identity.
Bone metastatic subclones and the reporter cell line were authenticated by the labs that developed them. Results with reporter and bone metastatic clones were confirmed with parental authenticated cell lines. All cell lines were re-authenticated by phenotype and morphology on arrival to our lab.

Mycoplasma contamination

All cell lines were negative for mycoplasma. Mycoplasma testing is done in our lab on a 6-month basis.

Commonly misidentified lines
(See ICLAC register)

No commonly misidentified cell lines were used.

Animals and other research organisms

Policy information about studies involving animals; ARRIVE guidelines recommended for reporting animal research, and Sex and Gender in Research

Laboratory animals

For the detection of disseminated tumor cells, five-to-six-week-old female athymic nude-Fox1nu mice were used. For in vivo tumor formation, six-to-eight-week-old female athymic nude-Fox1nu mice were used. The animals were housed no more than 5 per standard cage with ad-libitum water and chow in ambient temperature of 70–74° F, humidity of 30–70%, and a light–dark cycle of 14-hours on and 10-hours off.

Wild animals

The study did not involve wild animals

Reporting on sex

All animals used in this study were female.

Field-collected samples

The study did not involve samples collected from the field.

Ethics oversight

The animal studies were performed in accordance with Cornell University animal care guidelines and was approved by Cornell University's Institutional Animal Care and Use Committee under protocol number 2011-0006.

Note that full information on the approval of the study protocol must also be provided in the manuscript.

Flow Cytometry

Plots

Confirm that:

☒ The axis labels state the marker and fluorochrome used (e.g. CD4-FITC).

☒ The axis scales are clearly visible. Include numbers along axes only for bottom left plot of group (a 'group' is an analysis of identical markers).

☒ All plots are contour plots with outliers or pseudocolor plots.

☒ A numerical value for number of cells or percentage (with statistics) is provided.

Methodology

Sample preparation	Cells cultured on tissue-culture polystyrene were trypsinized, whereas cells on collagen and mineralized collagen were isolated using collagenase Type I. Suspended cells were passed through a 40-µm cell strainer, centrifuged, and resuspended in flow-cytometry buffer containing propidium iodide for subsequent flow cytometry.
Instrument	BD Accuri C6 Plus, BD Biosciences.
Software	FCS Express 6.06.0042
Cell population abundance	At least 10,000 cells were recorded for the analysis.
Gating strategy	Cells were gated by FSC and SSC, then FSC-A and FSC-H signals were used for doublet exclusion. Live cells were gated by PI signals. Cell populations expressing GFP from Nanog-GFP or ALDH from MDA-MB231 were analysed.

☒ Tick this box to confirm that a figure exemplifying the gating strategy is provided in the Supplementary Information.